

Cluster Structures of the Ground and Excited States of ^{12}Be Studied with Antisymmetrized Molecular Dynamics

Y. Kanada-En'yo

*Institute of Particle and Nuclear Studies,
High Energy Accelerator Research Organization,
Ibaraki 305-0801, Japan*

H. Horiuchi

Department of Physics, Kyoto University, Kyoto 606-8502, Japan

The structures of the ground and excited states of ^{12}Be were studied with antisymmetrized molecular dynamics. The ground state was found to be a state with a developed 2α core with two neutrons occupying the intruder orbits. The energy levels of the newly measured spin-assigned states were described well, except for the 1_1^- state. The calculations indicated that many exotic cluster structures appear in the low-energy region. The widths concerning α and ^6He decays were discussed by using reduced width amplitudes.

I. INTRODUCTION

Owing to the progress of experimental techniques, information concerning the excited states of light unstable nuclei has rapidly increased. Recently, exotic clustering in the light unstable nuclei has become one of the attractive subjects in experimental and theoretical research. Since, in light stable nuclei, it has already been known that clustering is one of the essential features of nuclear dynamics, not only in excited states, but also in ground states, it is natural to expect cluster features in light unstable nuclei. Pioneering theoretical studies have suggested the development of cluster structures with a 2α core in Be and B isotopes [1,2,3,4,5,6,7,8,9,10,11,19]. Especially, highly excited states with developed cluster structures in ^{10}Be and ^{11}Be have been studied by microscopic calculations [6,7,8,9,10,11]. In the case of ^{12}Be , the existence of cluster states was suggested in experimental measurements of the excited states [12]. In recent experiments of $^6\text{He}+^6\text{He}$ and $^4\text{He}+^8\text{He}$ breakup reactions [13,14], many new excited states were discovered above the threshold energies. Some of the states are candidates of exotic cluster states, since the measured spin-parities of those excited states indicate a rotational band with a large moment of inertia. It is an interesting subject to investigate clustering aspects in ^{12}Be . Although the molecular states in ^{12}Be were theoretically suggested with a potential model with He clusters [15], they have not yet been studied by microscopic calculations. The ground and the low-lying states of ^{12}Be present us with other attractive subjects concerning the vanishing of a neutron magic number, 8. The vanishing of the neutron magic number is already known in a neighboring nucleus, ^{11}Be . In ^{12}Be , the vanishing is supported by a recent measurement of the spin-parity for a low-lying 1^- state [16]. The recently observed low-lying 0_2^+ state [17] is also important to solve the inversion mechanism. Also, in theoretical studies, an abnormal structure of the ground state was suggested in an analysis of the beta-decay strength from the ground state of ^{12}Be into ^{12}B by T. Suzuki et al. [18]. The ground state, which has two neutrons in the intruder orbits, was microscopically described by a molecular-orbital model by N. Itagaki et al. [9], and by a method of antisymmetrized molecular dynamics by one of the authors (Y.K.) [19].

Our aim is to conduct systematic research of the structures of the ground and excited states of ^{12}Be based on microscopic theoretical calculations while focusing on clustering aspects. First of all, we have studied the systematics of the level structures, including the experimentally observed excited states. We have searched for cluster and non-cluster states to solve the following problems concerning clustering aspects in ^{12}Be . Do their cluster structures appear in ^{12}Be ? If they do appear, what are the characteristics of their structures in unstable nuclei compared with those of stable nuclei? The roles of the valence nucleons in the cluster states are interesting problems. We have also investigated the mechanism of the development and breaking of clustering.

The important point is that the theoretical approach should be free from model assumptions, such as the stability of the mean-field and the existence of inert cores or clusters, because we have to describe various structures covering developed cluster structures as well as shell-model-like structures in the ground and excited states. It is difficult to study developed clustering in excited states with such mean-field approaches as the traditional shell model and the Hartree-Fock model. The cluster structures of the excited states of ^9Be and ^{10}Be were successfully explained by cluster models [1,4,8,10,20] while assuming a 2α core and surrounding neutrons. However, we think that a description based on cluster models simplifying the system as a 2α core with valence neutrons or 2-He clusters is not sufficient for a systematic investigation of ^{12}Be because of many valence neutrons in the system. We have applied a theoretical approach of antisymmetrized molecular dynamics (AMD). The AMD method has already proved to be a useful

theoretical approach for the nuclear structure [2,5,7,11,21,22]. Within the AMD framework, we do not need such model assumptions as inert cores, clusters, or axial symmetries, because the wave function of the nuclear system is written by Slater determinants, where the spatial part of each single-particle wave function for a nucleon is expressed by a localized Gaussian wave packet. Due to the flexibility of the AMD wave function, we successfully described the structure changes between shell-model-like states and cluster states as functions of the neutron number in light unstable nuclei. Owing to progress in computational power, it has become possible to study excited states by extended AMD calculations. This method is based on variational calculation after spin-parity projection (VAP calculation) within the framework of AMD, which has already been confirmed to be powerful for studying the excited states of light nuclei, as shown in studies of the stable nucleus ^{12}C [22], and also unstable nuclei (^{10}Be and ^{11}Be) [7,11]. The authors and their collaborators succeeded to describe various structures of the excited states and to reproduce many kinds of experimental data for nuclear structures of these nuclei with the AMD method.

In the present work, the structures of the ground and excited states of ^{12}Be were analyzed by performing a variational calculation after spin-parity projection based on the AMD method. In the next section (Sec. II), we explain the formulation of AMD for a study of the nuclear structure of excited states. The adopted effective interactions are explained in Sec. III. In Sec. IV, we present the calculated results concerning such observables as the energy levels, radii and β decays as well as the $E1$ and $E2$ transitions compared with the experimental data. In the discussion (Sec. V), the intrinsic structures and the rotational band structures are described. The single-particle behavior of the valence neutrons is analyzed. We discuss the systematics of the development of cluster states in Be isotopes, which can be classified according to the neutron orbits surrounding the 2α core. We investigate the inter-cluster motions between He clusters extracted from the obtained ^{12}Be wave functions, and calculate the decay widths for the ^4He and ^6He channels by using the method of reduced width amplitudes.

II. FORMULATION

In this section, the formulation of AMD for a nuclear structure study of ground and excited states is briefly explained. For more detailed descriptions of the AMD framework, the reader is referred to Refs. [2,7,22].

A. Wave function

The wave function of a system is written by a superposition of the AMD wave functions,

$$\Phi = c\Phi_{AMD} + c'\Phi'_{AMD} + \dots \quad (1)$$

The AMD wave function of a nucleus with a mass number A is a Slater determinant of Gaussian wave packets:

$$\Phi_{AMD}(\mathbf{Z}) = \frac{1}{\sqrt{A!}} \mathcal{A}\{\varphi_1, \varphi_2, \dots, \varphi_A\}, \quad (2)$$

$$\varphi_i = \phi_{\mathbf{x}_i} \chi_{\xi_i} \chi_{\tau_i} : \begin{cases} \phi_{\mathbf{x}_i}(\mathbf{r}_j) \propto \exp[-\nu(\mathbf{r}_j - \frac{\mathbf{x}_i}{\sqrt{\nu}})^2], \\ \chi_{\xi_i} = \begin{pmatrix} \frac{1}{2} + \xi_i \\ \frac{1}{2} - \xi_i \end{pmatrix}, \end{cases} \quad (3)$$

where the i th single-particle wave function (φ_i) is a product of the spatial wave function ($\phi_{\mathbf{x}_i}$), the intrinsic spin function (χ_{ξ_i}) and the iso-spin function (χ_{τ_i}). The spatial part ($\phi_{\mathbf{x}_i}$) is presented by variational complex parameters, X_{1i} , X_{2i} , X_{3i} . χ_{ξ_i} is the intrinsic spin function, defined by ξ_i , and τ_i is an iso-spin function which is fixed to be up(proton) or down(neutron) in the present calculations. Thus, an AMD wave function is expressed by a set of variational parameters, $\mathbf{Z} \equiv \{X_{ni}, \xi_i\}$ ($n = 1, 2, 3$ and $i = 1, \dots, A$), which indicate the centers of Gaussians of the spatial part and the spin directions of the intrinsic spin part of the single-particle wave functions.

When we consider a parity eigen state projected from an AMD wave function, the total wave function is written by two Slater determinants,

$$\Phi(\mathbf{Z}) = (1 \pm P)\Phi_{AMD}(\mathbf{Z}), \quad (4)$$

where P is the parity projection operator. In the case of a total-angular-momentum eigen state, the wave function of the state is represented by the integral of the rotated AMD wave functions,

$$\Phi(\mathbf{Z}) = P_{MK}^J \Phi_{AMD}(\mathbf{Z}) = \int d\Omega D_{MK}^{J*}(\Omega) R(\Omega) \Phi_{AMD}(\mathbf{Z}), \quad (5)$$

where the function D_{MK}^J is the well-known Wigner's D function and $R(\Omega)$ stands for the rotation operator with Euler angle Ω .

In principle, the total wave function can be a superposition of independent AMD wave functions. We can make the superposition of the spin-parity projected AMD wave functions ($P_{MK'}^{J\pm}\Phi_{AMD}$) as follows:

$$\Phi = cP_{MK'}^{J\pm}\Phi_{AMD}(\mathbf{Z}) + c'P_{MK'}^{J\pm}\Phi_{AMD}(\mathbf{Z}') + \dots \quad (6)$$

The expectation values of a given tensor operator, T_q^k (rank k), for the total-angular-momentum projected states $P_{M_1K_1}^{J_1\pm}\Phi_{AMD}(\mathbf{Z})$ and $P_{M_2K_2}^{J_2\pm}\Phi_{AMD}(\mathbf{Z}')$ are calculated as follows:

$$\langle P_{M_1K_1}^{J_1\pm}\Phi_1 | T_q^k | P_{M_2K_2}^{J_2\pm}\Phi_2 \rangle \quad (7)$$

$$= \frac{2J_2+1}{8\pi^2} (J_2M_2kq | J_1M_1) \sum_{K\nu} (J_2Kk\nu | J_1K_1) \int d\Omega D_{KK_2}^{J_2*}(\Omega) \langle \Phi_1 | T_\nu^k R(\Omega) | \Phi_2 \rangle. \quad (8)$$

The integral can be evaluated by summing over mesh points of the Euler angles (Ω).

B. Energy variation

We performed a variational calculation for a trial wave function to find the state which minimizes the energy of the system,

$$\frac{\langle \Phi | H | \Phi \rangle}{\langle \Phi | \Phi \rangle} \quad (9)$$

by the method of frictional cooling, which is one of the imaginary time methods. Regarding the frictional cooling method in AMD, the reader is referred to two papers [2,21]. The time development of the parameters \mathbf{Z} of the wave function $\Phi(\mathbf{Z})$ are given by the frictional cooling equations, as follows:

$$\frac{dX_{nk}}{dt} = (\lambda + i\mu) \frac{1}{i\hbar} \frac{\partial}{\partial X_{nk}^*} \frac{\langle \Phi(\mathbf{Z}) | H | \Phi(\mathbf{Z}) \rangle}{\langle \Phi(\mathbf{Z}) | \Phi(\mathbf{Z}) \rangle} \quad (n = 1, 3 \quad k = 1, A), \quad (10)$$

$$\frac{d\xi_k}{dt} = (\lambda + i\mu) \frac{1}{i\hbar} \frac{\partial}{\partial \xi_k^*} \frac{\langle \Phi(\mathbf{Z}) | H | \Phi(\mathbf{Z}) \rangle}{\langle \Phi(\mathbf{Z}) | \Phi(\mathbf{Z}) \rangle} \quad (k = 1, A), \quad (11)$$

with arbitrary real numbers λ and $\mu < 0$. It is easily proved that the energy of the system decreases with time due to the frictional term, μ . After sufficient time steps of cooling, the minimum-energy state is obtained.

C. Wave functions of J^\pm states

In order to obtain the wave function for the lowest J^\pm state, we varied the parameters \mathbf{X}_i and ξ_i ($i = 1 \sim A$) to minimize the energy expectation value of a spin-parity projected AMD wave function, $\Phi = P_{MK'}^{J\pm}\Phi_{AMD}(\mathbf{Z})$, by using the frictional cooling method mentioned above. That is to say, we performed energy variation after spin-parity projection(VAP) for an AMD wave function.

With the VAP calculation for the J^\pm eigen state, $\Phi_1^{J\pm}(\mathbf{Z}) = P_{MK'}^{J\pm}\Phi_{AMD}(\mathbf{Z})$, with an appropriate K' , we obtained a set of parameters, $\mathbf{Z} = \mathbf{Z}_1^{J\pm}$, which presents the wave function of the first J^\pm state. In order to search for the parameters $\mathbf{Z} = \mathbf{Z}_n^{J\pm}$ of the n th J^\pm state, the wave functions were superposed so as to be orthogonal to the lower states. The parameters $\mathbf{Z}_n^{J\pm}$ for the n th J^\pm state were provided by varying \mathbf{Z} so as to minimize the energy of the wave function orthogonalized to the lower states,

$$\Phi_n^{J\pm}(\mathbf{Z}) = P_{MK'}^{J\pm}\Phi_{AMD}(\mathbf{Z}) - \sum_{k=1}^{n-1} \frac{\langle \Phi_k^{J\pm}(\mathbf{Z}_k^{J\pm}) | P_{MK'}^{J\pm}\Phi_{AMD}(\mathbf{Z}) \rangle}{\langle \Phi_k^{J\pm}(\mathbf{Z}_k^{J\pm}) | \Phi_k^{J\pm}(\mathbf{Z}_k^{J\pm}) \rangle} \Phi_k^{J\pm}(\mathbf{Z}_k^{J\pm}). \quad (12)$$

D. Diagonalization

After the VAP calculation of the J_n^π states for various J , n and $\pi = \pm$, we obtained the optimum intrinsic states, $\Phi_{AMD}(\mathbf{Z}_n^{J^\pi})$, which approximately describe the corresponding J_n^π states. In order to obtain more precise wave functions, we superposed the spin-parity eigen wave functions projected from all of the obtained intrinsic states. Namely, we determined the final wave functions for the J_n^\pm states by simultaneously diagonalizing the Hamiltonian matrix, $\langle P_{MK'}^{J^\pm} \Phi_{AMD}(\mathbf{Z}_{n_i}^{J_i^\pi}) | H | P_{MK''}^{J^\pm} \Phi_{AMD}(\mathbf{Z}_{n_j}^{J_j^\pi}) \rangle$, and the norm matrix, $\langle P_{MK'}^{J^\pm} \Phi_{AMD}(\mathbf{Z}_{n_i}^{J_i^\pi}) | P_{MK''}^{J^\pm} \Phi_{AMD}(\mathbf{Z}_{n_j}^{J_j^\pi}) \rangle$, with regard to (i, j) for all of the obtained intrinsic states, and to (K', K'') . Compared with the experimental data, such as the energy levels and $E2$ transitions, the expectation values were calculated with the final states after diagonalization.

III. INTERACTIONS

The adopted interaction is the sum of the central force, the spin-orbit force and the Coulomb force. The central force is chosen to be the MV1 force of case 3 [23], which contains a zero-range three-body force, $V^{(3)}$, as a density-dependent term in addition to the two-body interaction, $V^{(2)}$, of the modified Volkov No.1 force. The spin-orbit force of the G3RS force [24] is adopted.

IV. RESULTS

The structures of the excited states of ^{12}Be were studied based on the VAP calculation within the framework of AMD. In this section, we present theoretical results, such as the energy levels, radii, and transitions (β , $E2$, $E1$ and $E0$), while comparing them with the experimental data. A detailed analysis of the structures of the states is given in the next section.

The adopted interaction parameters in the present work are those used in Refs. [7,11], which reproduced the abnormal spin-parity $1/2^+$ of the ground state of ^{11}Be . Namely, the Majorana, Bartlett and Heisenberg parameters in the central force are $m = 0.65$, $b = h = 0$, and the strength of the spin-orbit force is chosen to be $u_I = -u_{II} = 3700$ MeV. The width parameter (ν) was chosen to be 0.17 fm^{-2} , which gave a minimum energy of ^{12}Be in a simple AMD calculation without the spin projection.

The wave functions for the lowest J^\pm states were obtained by the VAP calculation of $P_{MK'}^{J^\pm} \Phi_{AMD}$ by choosing $(J^\pm, K') = (0^+, 0)$, $(2^+, 0)$, $(4^+, 0)$, $(6^+, 0)$, $(8^+, 0)$, $(1^-, 1)$, $(2^-, 1)$, $(3^-, 1)$, $(4^-, 1)$, $(5^-, 1)$, $(6^-, 1)$, $(3^+, 2)$, $(5^+, 2)$, $(7^+, 2)$, $(0^-, 0)$, $(1^+, 1)$, $(1^+, 0)$. After obtaining the lowest states (J_1^\pm), we calculated the second and third J^\pm states (0_2^+ , 0_3^+ , 2_2^+ , 2_3^+ , 4_2^+ , 6_2^+ , 1_2^-) with the VAP calculation of the superposed wave functions orthogonal to the obtained lower J^\pm states. The obtained AMD wave functions are considered to approximately describe the intrinsic states of the corresponding J_n^\pm states. The final wave functions of the J_n^\pm states were determined by superposing the spin-parity eigen states projected from these obtained AMD wave functions so as to simultaneously diagonalize the Hamiltonian matrix and the norm matrix. In principle, the number of the superposed AMD wave functions is 24, which is the number of calculated levels. In the present calculations, we omitted several of them which are not important, just to save computational time. Namely, we diagonalize the positive-parity(negative-parity) states projected from 22(18) AMD wave functions.

A. Energies

The theoretical binding energy of ^{12}Be was found to be 61.9 MeV(60.4 MeV) after(before) diagonalization, which underestimated the experimental value, 68.65 MeV. We found that the binding could be improved by changing the Majorana parameter (m) of the interaction to a smaller value. For example, a theoretical value of 66.1 MeV was obtained by using $m = 0.62$ with a simple VAP calculation before diagonalization. Nevertheless, we adopted the parameter $m = 0.65$ in the present work, because this value reproduces the parity inversion of ^{11}Be [11], which should be important for describing the ground-state properties of the neighboring nucleus, ^{12}Be . We checked that the change in the m parameter has no significant effect on the excitation energies, $E(0_2^+)$ and $E(8_1^+)$, of ^{12}Be , at least. In fact, the calculated excitation energies of $E(0_2^+)$ before diagonalization are 3.0 MeV and 2.8 MeV, in the cases of $m = 0.62$ and $m = 0.65$, respectively.

The theoretical level scheme is shown in Fig.1. The calculations suggest that many excited states appear in the low-energy region. This is the first theoretical work which systematically reproduces the experimental energy levels of all the spin-assigned states, except for the 1^- state. By analyzing the intrinsic AMD wave functions of the states, we

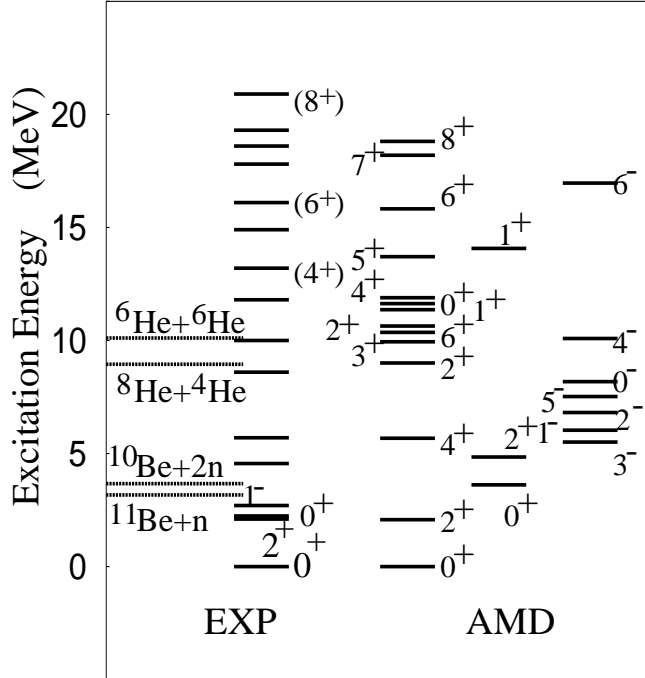


FIG. 1. Excitation energies of the levels in ^{12}Be . The experimental data are from the Table of Isotopes and Refs. [13,16,12,14,17].

can consider that there exist rotational bands ($K^\pi=0_1^+$, 0_2^+ , 0_3^+ and 1_1^-), which consist of the following states: $\{0_1^+$, 2_1^+ , 4_1^+ , 6_1^+ and $8_1^+\}$, $\{0_2^+$, $2_2^+\}$, $\{0_3^+$, 2_3^+ , 4_2^+ , 6_2^+ and $8_1^+\}$ and $\{1_1^-$, 2_1^- , 3_1^- , 4_1^- , $5_1^-\}$, respectively

The energy-spin systematics for positive-parity states with natural spins are shown in Fig. 2. It is surprising that the newly observed levels, 4^+ at 13.2 MeV and 6^+ at 16.1 MeV [13], correspond well to the 4_2^+ and 6_2^+ states in the theoretical results. An interesting point is that these excited states belong not to the yrast band, $K^\pi = 0_1^+$, but to the excited $K^\pi = 0_3^+$ band, which is a new band other than the ground band. The theoretical results predict the existence of many positive-parity states belonging to the $K^\pi = 0_1^+$ and $K^\pi = 0_2^+$ bands in the lower energy region. Even though ^{12}Be has a neutron magic number of 8, the calculated ground $K^\pi = 0^+$ band has a large moment of inertia, because the band head 0_1^+ state is not the ordinary state with a closed neutron p -shell, but an intruder state with a developed cluster structure. It has a prolate deformed structure, which is dominated by $2p$ - $2h$ configurations, and reaches the band terminal at the 8_1^+ state. The third 0^+ band ($K^\pi = 0_3^+$) was found to be represented by other $2p$ - $2h$ configurations than those in the $K^\pi = 0_1^+$ band. The $K^\pi = 0_3^+$ band has an extremely large moment of inertia because of a remarkably developed $^6\text{He}+^6\text{He}$ clustering, and reaches the band terminal 8_1^+ state accompanying the spin-alignment of nucleons in the high-spin region. The rotational bands, $K^\pi = 0_3^+$ and $K^\pi = 0_1^+$, terminate with the same state, because the $J^\pm = 8_1^+$ state is the unique highest-spin state in the $2\hbar\omega$ excited configurations. On the other hand, the main components of the 0_2^+ and 2_2^+ states are of the $0\hbar\omega$ configuration, with the closed neutron p -shell, and constitute the $K^\pi = 0_2^+$ band. The band head 0_2^+ state of this band, which was theoretically predicted to appear just above the intruder ground band by Itagaki et al. [8] and Kanada-En'yo et al. [28], was recently discovered in an observation of coincidence gamma rays by Shimoura et al. [17].

The theoretical excitation energy of the 1_1^- state is larger than the measured 1^- state at 2.68 MeV [16]. In spite of the overestimation of the excitation energy, we regard this 1_1^- state in the $K^\pi = 1^-$ as the 1^- state at 2.68 MeV because of the large $E1$ transition strength, as shown later.

B. Radii

The theoretical values of the root-mean-square radii of the density distributions of point-like nucleons, protons, and neutrons are listed in Table I together with the experimental matter radius [25] deduced from the reaction cross sections. Because of deformations, the proton and neutron radii in the ground state are larger compared with those

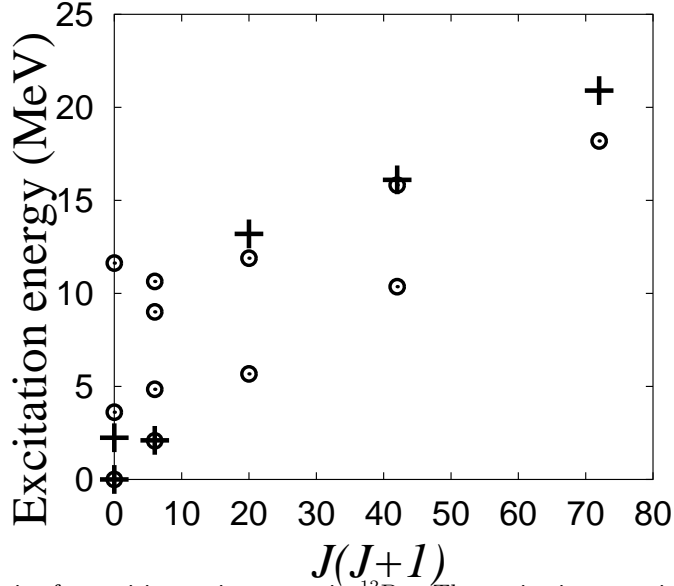


FIG. 2. Energy-spin systematics for positive-parity states in ^{12}Be . The excitation energies of the natural spin states are plotted as functions of $J(J+1)$. The circle symbols are the theoretical results, while the cross symbols are the experimental data of the spin-parity assigned states, which are taken from the Table of Isotopes and Refs. [13,17].

TABLE I. The root-mean-square radii of the density distribution of point-like nucleons, protons, and neutrons. The experimental matter radius deduced from the reaction cross sections is taken from Ref. [25].

	matter	proton	neutron
$^{12}\text{Be}(0_1^+)$	2.85 fm	2.67 fm	2.94 fm
$^{12}\text{Be}(0_2^+)$	2.75 fm	2.56 fm	2.84 fm
exp.	2.59 ± 0.06	–	–

in the 0_2^+ state. Since the theoretical values concerning the difference $\Delta r = r_n - r_p$ between the proton and neutron radii are about 0.3 fm, ^{12}Be is a candidate of the neutron skin nucleus. Compared with the experimental data, the present result for 0_1^+ is larger because the present parameter $m = 0.65$ is considered to be too large to quantitatively reproduce the radii of p -shell nuclei.

The proton and neutron densities as functions of the radius are shown in Fig. 3. In both the 0_1^+ and 0_2^+ states, the excess neutrons enhance the neutron density in the surface region. In the 0_1^+ state, due to cluster development, the proton density increases in the surface region while it decreases at the center of the nucleus. It should be noted that, even if a nucleus has a neutron halo (the long tail of the neutron density in the outer region), the details of the halo structure are not expressed in the present model space because of a limitation of the Gaussian forms in AMD wave functions.

C. β decay strength

The strength of the β decay from $^{12}\text{Be}(0_1^+)$ to $^{12}\text{B}(1^+)$ provides helpful experimental evidence for breaking of the neutron p -shell closure in $^{12}\text{Be}(0_1^+)$. T. Suzuki et al. suggested that weak β decay is experimental evidence for an admixture of non- $0\hbar\omega$ configurations in $^{12}\text{Be}(0_1^+)$, because the β decays from a normal p -closed state of $^{12}\text{Be}(0_1^+)$ must be stronger. We calculated the Gamow-Teller transition strength, $B(GT) \equiv |\langle\sigma\tau\rangle|^2$, where the wave function for the daughter state, $^{12}\text{B}(1_1^+)$, was obtained by a VAP calculation with $(J^\pm, K') = (1^+, -1)$. The $B(GT)$ values are given shown in Table II. The present result, $B(GT) = 0.9$, is almost as small as the experimental data, $B(GT) = 0.59$, because the component of the $2\hbar\omega$ configurations in the parent $^{12}\text{Be}(0_1^+)$ makes the transition matrix element of the Gamow-Teller operator to be small. In fact, the original 0_1^+ state of ^{12}Be obtained by a simple VAP calculation before diagonalization has very weak β transitions as $B(GT : ^{12}\text{Be}(0_1^+) \rightarrow ^{12}\text{B}(1_1^+)) = 0.2$. On the other hand, the decay from

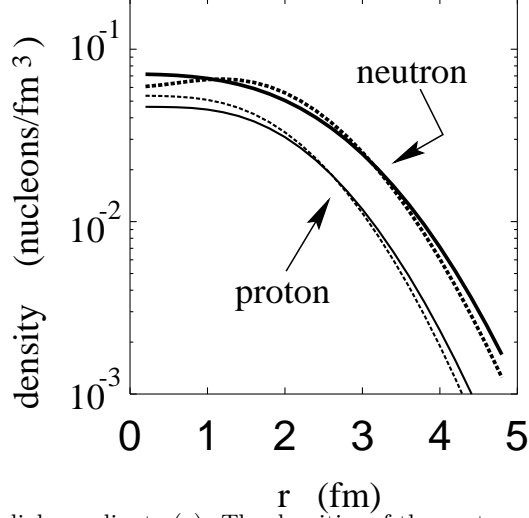


FIG. 3. Densities as functions of the radial coordinate (r). The densities of the protons and neutrons in the 0_1^+ state (solid) and in the 0_2^+ state (dashed) are shown.

TABLE II. The strength of β decays. $B(GT)$ is defined as $|\langle\sigma\tau\rangle|^2$. The experimental data are taken from [26].

initial (J^π, E_x) (MeV)	final (J^π, E_x) (MeV)	B(GT)	
$^{12}\text{Be}(0^+, 0)$	$^{12}\text{B}(1^+, 0)$	exp.	0.56
		theory	
		before diagonalization	after diagonalization
$^{12}\text{Be}(0_1^+)$	$^{12}\text{B}(1_1^+)$	0.2	0.9
$^{12}\text{Be}(0_2^+)$	$^{12}\text{B}(1_1^+)$	3.0	2.1
$^{12}\text{Be}(0_3^+)$	$^{12}\text{B}(1_1^+)$	0.05	0.07
$^{12}\text{Be}(2_1^+)$	$^{12}\text{B}(1_1^+)$	0.004	0.1
$^{12}\text{Be}(2_2^+)$	$^{12}\text{B}(1_1^+)$	0.5	0.4

0_2^+ is strong as $B(GT : ^{12}\text{Be}(0_2^+) \rightarrow ^{12}\text{B}(1_1^+)) = 3.0$ before diagonalization, because the parent state has the ordinary $0\hbar\omega$ configuration. After state mixing with diagonalization, the GT strength from $^{12}\text{Be}(0_2^+)$ is distributed to that from $^{12}\text{Be}(0_1^+)$. As a result, after the diagonalization the $B(GT : ^{12}\text{Be}(0_1^+) \rightarrow ^{12}\text{B}(1_1^+))$ value increases to 0.9, while $B(GT : ^{12}\text{Be}(0_2^+) \rightarrow ^{12}\text{B}(1_1^+))$ decreases to 2.1. According to the present results, the GT transitions from $^{12}\text{Be}(0_3^+)$ are weak, while the $B(GT : ^{12}\text{Be}(2_2^+) \rightarrow ^{12}\text{B}(1_1^+))$ is largest among the 2^+ states because the 2_2^+ state is the other $0\hbar\omega$ state belonging to the $K^\pi = 0_2^+$ band.

The present results concerning the weak GT decay from the ground state is consistent with the discussion given by T. Suzuki et al. [18]. The point of the present work is that the ground state property of ^{12}Be is described based on a fully microscopic calculation.

D. $E2, E1, E0$ transition strength

Although the data concerning the $E2$ transition strength provide good information about proton deformations, we must take care of the following points in the analysis of light neutron-rich nuclei. Firstly, it is dangerous to assume the same deformation of the proton density as that of the neutron density in light unstable nuclei. Secondly, the classical relations between the intrinsic deformation (Q_0) and the observables, which are often used in a simple analysis of heavy nuclei, do not necessarily work in light nuclei. Therefore, it is necessary to analyze the transition strength based on a microscopic calculation. As shown in previous AMD studies [2,22,7], the experimental Q -moments and $B(E2)$

TABLE III. Theoretical results of $E2$, $E1$ and $E0$ transition strength, $B(E\lambda)$. $B(E0)$ is defined as $|\langle f | \frac{1+\tau}{2} r^2 | i \rangle|$.

transitions	band(K^π)	Mult.	present
$^{12}\text{Be}; 2_1^+ \rightarrow 0_1^+$	in 0_1^+	$E2$	14 ($e^2 \text{ fm}^4$)
$^{12}\text{Be}; 2_2^+ \rightarrow 0_2^+$	in 0_2^+	$E2$	8 ($e^2 \text{ fm}^4$)
$^{12}\text{Be}; 2_4^+ \rightarrow 0_3^+$	in 0_3^+	$E2$	8 ($e^2 \text{ fm}^4$)
$^{12}\text{Be}; 4_1^+ \rightarrow 2_1^+$	in 0_1^+	$E2$	14 ($e^2 \text{ fm}^4$)
$^{12}\text{Be}; 4_2^+ \rightarrow 2_4^+$	in 0_3^+	$E2$	10 ($e^2 \text{ fm}^4$)
$^{12}\text{Be}; 4_1^+ \rightarrow 2_2^+$		$E2$	5 ($e^2 \text{ fm}^4$)
$^{12}\text{Be}; 4_2^+ \rightarrow 2_1^+$		$E2$	5 ($e^2 \text{ fm}^4$)
$^{12}\text{Be}; 4_2^+ \rightarrow 2_3^+$		$E2$	6 ($e^2 \text{ fm}^4$)
$^{12}\text{Be}; 0_1^+ \rightarrow 1_1^-$		$E1$	2×10^{-2} ($e^2 \text{ fm}^2$)
$^{12}\text{Be}; 0_2^+ \rightarrow 1_1^-$		$E1$	2×10^{-2} ($e^2 \text{ fm}^2$)
$^{12}\text{Be}; 0_2^+ \rightarrow 0_1^+$		$E0$	1.7 ($e \text{ fm}^2$)

values of light nuclei were reproduced well by using bare charges, because of the advantage of the AMD method, which can directly express the proton and neutron deformations.

Table III gives the theoretical $B(E2)$, $B(E1)$ and $B(E0)$ values calculated by the VAP calculation after diagonalization. The intra-band $E2$ transitions in the $K^\pi = 0_1^+$ band are strong, as seen in $B(E2; 2_1^+ \rightarrow 0_1^+) = 14 e^2 \text{ fm}^4$, due to the deformed intrinsic state. On the other hand, $B(E2)$ is smaller in the transition between the 2_2^+ and 0_2^+ states in the $K^\pi = 0_2^+$ band, which have rather spherical shapes compared to those in the $K^\pi = 0_1^+$ band. Although the deformations of the states in the $K^\pi = 0_3^+$ band are extremely large in the present results, $B(E2; 4_2^+ \rightarrow 2_4^+)$ and $B(E2; 2_4^+ \rightarrow 0_3^+)$ are not as large as those in the $K^\pi = 0_1^+$ band, because the intrinsic structure varies with increasing the total spin (J) along the 0_3^+ band. The $B(E2)$ values regarding the transitions between different bands are smaller compared with those for the intra-band transitions.

Compared with the experimental data, $B(E2; 2_1^+ \rightarrow 0_1^+) = 10.5 \pm 1.1 (e^2 \text{ fm}^4)$ of ^{10}Be , the present results predict a larger $B(E2)$ of ^{12}Be as $B(E2; 2_1^+ \rightarrow 0_1^+) = 14 e^2 \text{ fm}^4$. We should point out that the $E2$ transition strength is sensitive to the mixing ratio with the 0_2^+ and 2_2^+ states as well as deformations. Since the 0_2^+ and 2_2^+ states are suggested to exist just above the 0_1^+ and 2_1^+ states, we should more carefully investigate the energy difference and the state mixing between the $K^\pi = 0_1^+$ and $K^\pi = 0_2^+$ bands before making conclusion.

The $E1$ transition strength was recently measured as $B(E1; 1_1^- \rightarrow 0_1^+) = 0.05 e^2 \text{ fm}^2$ [16], which is rather large compared with other light nuclei. The calculated result, $B(E1; 1_1^- \rightarrow 0_1^+) = 0.02 e^2 \text{ fm}^2$, reasonably agrees with this experimental data. Before diagonalization, the deformed 0_1^+ state possesses the strength of the $E1$ transition from the 1_1^- state, while the transition to the spherical 0_2^+ state is weak. After diagonalization, the strength in the 0_1^+ state distributes in the 0_2^+ state due to state mixing between the 0_1^+ and the 0_2^+ states. In other words, the rather large $B(E1; 1_1^- \rightarrow 0_1^+)$ is caused by a deformation of the ground state.

V. DISCUSSIONS

In the present calculations, many deformed rotational bands appeared in ^{12}Be . It was found that 2α core is formed in most of the states as well as in other neutron-rich Be isotopes: ^{10}Be and ^{11}Be [6,7,11]. In this section, we consider the intrinsic structures of ^{12}Be while focusing on the clustering aspects and the behavior of the valence neutrons. The features of the intrinsic structures, the roles of valence neutrons and the inter-cluster motions in the cluster states are discussed.

A. Systematics of rotational bands

By analyzing the structures of the intrinsic states, we can classify the ground and excited states into rotational bands. We superpose the wave functions, $P_{MK}^{J^\pm} \Phi_{AMD}$, projected from all of the intrinsic wave functions, $\Phi_{AMD}(\mathbf{Z}_n^{J_i, \pi_i})$, obtained by VAP so as to diagonalize the Hamiltonian matrix. Nevertheless, we consider the AMD wave function, $\Phi_{AMD}(\mathbf{Z}_n^{J^\pm})$, before diagonalization as being the intrinsic state of the corresponding J^\pm state, because $P_{MK}^{J^\pm} \Phi_{AMD}(\mathbf{Z}_n^{J^\pm})$ is found to be the main component of the final result of the J_n^\pm state after diagonalization, except for the 2_3^+ and 2_4^+ states. For example, in the final wave functions of 0_1^+ , 0_2^+ and 0_3^+ after diagonalization, the

TABLE IV. The amplitudes of the corresponding $P_{MK}^{J^\pm} \Phi_{AMD}(\mathbf{Z}_{n_i}^{J_i \pi_i})$ VAP wave functions in the final wave functions obtained after the diagonalization.

J_n^+ after diagonalization	amplitude	$(J_i^{\pi_i}, K , n_i)$ in VAP
0_1^+	0.8	$(0^+, 0, 1)$
2_1^+	0.8	$(2^+, 0, 1)$
4_1^+	0.9	$(4^+, 0, 1)$
6_1^+	0.9	$(6^+, 0, 1)$
8_1^+	0.9	$(8^+, 0, 1)$
0_2^+	0.6	$(0^+, 0, 2)$
2_2^+	0.7	$(2^+, 0, 2)$
0_3^+	0.7	$(0^+, 0, 3)$
2_4^+	0.4	$(2^+, 0, 3)$
4_2^+	0.6	$(4^+, 0, 2)$
6_2^+	0.6	$(6^+, 0, 2)$
1_1^-	0.9	$(1^-, 1, 1)$
2_1^-	0.9	$(2^-, 1, 1)$
3_1^-	0.9	$(3^-, 1, 1)$
4_1^-	0.7	$(4^-, 1, 1)$
5_1^-	0.9	$(5^-, 1, 1)$
2_3^+	0.8	$(3^+, 2, 1)$
3_1^+	0.8	$(3^+, 2, 1)$
5_1^+	0.8	$(5^+, 2, 1)$
7_1^+	0.9	$(7^+, 2, 1)$
0_1^-	1.0	$(0^-, 0, 1)$
1_1^+	0.9	$(1^+, 1, 1)$
1_2^+	1.0	$(1^+, 0, 1)$
6_1^-	0.9	$(6^-, 1, 1)$

amplitudes of the original VAP states (0_1^+ , 0_2^+ and 0_3^+) are 0.8, 0.6 and 0.7, respectively. In Table IV, the amplitudes of the original states without superposition in the diagonalized final wave functions are listed. The amplitudes are larger than 0.6, except for the 1_2^- , 2_3^+ and 2_4^+ states. In the negative-parity state of 1_2^- , the component of the original state becomes less than 0.6 after diagonalization. Considering that this state might be unstable, we neglect the 1_2^- level in the present results. In the case of the 2_3^+ state, the main component of the 2_3^+ state is not the projected AMD state, $P_{M0}^{2+} \Phi_{AMD}(\mathbf{Z}_3^{2+})$, obtained by a VAP calculation for $J_n^\pm = 2_3^+$, but is the $P_{M2}^{2+} \Phi_{AMD}(\mathbf{Z}_1^{3+})$, which is projected from the intrinsic state of the 3_1^+ state. This means that a new 2^+ state appears in addition to three 2^+ states obtained by the VAP calculation, \mathbf{Z}_1^{2+} , \mathbf{Z}_2^{2+} and \mathbf{Z}_3^{2+}). The energy of this new 2^+ state, $P_{M2}^{2+} \Phi_{AMD}(\mathbf{Z}_1^{3+})$, is slightly lower than that of $P_{M0}^{2+} \Phi_{AMD}(\mathbf{Z}_3^{2+})$. As a result, the intrinsic wave functions, $\Phi_{AMD}(\mathbf{Z}_1^{3+})$ and $\Phi_{AMD}(\mathbf{Z}_3^{2+})$, are regarded to be the intrinsic states of the 2_3^+ and 2_4^+ states, respectively, although the amplitude of the original VAP state, $P_{M0}^{2+} \Phi_{AMD}(\mathbf{Z}_3^{2+})$, in the 2_4^+ state is as small as 0.4 after diagonalization because of mixing the 2_3^+ state with the 2_4^+ state. The reason why the intrinsic state of the 2_3^+ state is not obtained in the VAP calculation with $(J^\pm, K') = (2^+, 0)$ is considered to be because the 2_3^+ state belongs to $K^\pi = 2^+$.

By analyzing the intrinsic states, we find the rotational bands $K^\pi = 0_1^+, 0_2^+, 0_3^+, 2_1^+, 1_1^-$, which consist of the states $(0_1^+, 2_1^+, 4_1^+, 6_1^+, 8_1^+)$, $(0_2^+, 2_2^+)$, $(0_3^+, 2_4^+, 4_2^+, 6_2^+, 8_1^+)$, $(2_3^+, 3_1^+, 5_1^+, 7_1^+)$, and $(1_1^-, 2_1^-, 3_1^-, 4_1^-, 5_1^-)$, respectively. We analyze the parity-eigen components in the single-particle wave functions of the intrinsic states, and find that each rotational band is dominated by either the $0\hbar\omega$, $1\hbar\omega$ or $2\hbar\omega$ excited configuration. The states in the three positive-parity bands ($K^\pi = 0_1^+, 0_3^+, 2_1^+$) have the dominant $2\hbar\omega$ excited configurations. The first interesting point is that the states in the ground band are not the closed neutron-shell states, but are the prolately deformed intruder states with developed clustering, even though this ^{12}Be nucleus has a neutron magic number of $N = 8$. This is consistent with discussions of the vanishing of the neutron magic number in ^{12}Be given by Refs. [9,16,18]. Because of the $2\hbar\omega$ excited configurations, the $K^\pi = 0_1^+$ band starting from the 0_1^+ state terminates with the 8_1^+ state. On the other hand, the present results predict that the 0_2^+ and 2_2^+ states with the dominant $0\hbar\omega$ configurations constitute the excited band, $K^\pi = 0_2^+$, just above the ground band. The second interesting point is that the newly observed levels, 4^+ and 6^+ states [13], are considered to belong to the third rotational $K^\pi = 0_3^+$ band, which is the higher one of the two $2\hbar\omega$ bands, $K^\pi = 0_1^+$ and $K^\pi = 0_3^+$, with developed cluster structures. The $K^\pi = 0_3^+$ band terminates with the same state as that of the

$K^\pi = 0_1^+$ band, because the $J^\pm = 8_1^+$ state is the unique highest-spin state in the $2\hbar\omega$ configurations. The $K^\pi = 2_1^+$ band consists of the $2_3^+, 3_1^+, 5_1^+, 7_1^+$ states, which have the other $2\hbar\omega$ configurations. Although spin-parity eigen states, 4^+ and 6^+ , are able to be projected from the intrinsic states of this $K^\pi = 2_1^+$ band in principle, the 4^+ and 6^+ states in the $K^\pi = 2_1^+$ band can not be identified, because these states strongly mix with the $4_1^+, 4_2^+, 6_1^+$ and 6_2^+ states in the $K^\pi = 0_1^+$ and $K^\pi = 0_3^+$ bands. The reason for the unnatural spin-parity of these states is the component of the total neutron-intrinsic spins, $S_n = 1$. We find a negative-parity band, $K^\pi = 1_1^-$, in which the states ($1^-, 2^-, 3^-, 4^-, 5^-$) are dominated by $1\hbar\omega$ configurations.

B. Intrinsic structures

We discuss the features of the intrinsic structures, such as the deformations and clustering aspects. The density distributions of the intrinsic AMD wave functions are shown in Fig. 4.

In most of the states, except for the $2_2^+, 5_1^-$ and 1_2^+ states, the densities of protons have dumbbell-like shapes, which indicate the formation of a 2α core. On the other hand, 2α core breaking occurs in the $2_2^+, 5_1^-$ and 1_2^+ states. For the quantitative discussions, we can estimate the degree of core breaking based on the non-zero values of the squared total-intrinsic spin of protons, $\langle \mathbf{S}_p^2 \rangle$, given in table V. In most of the states, the values $\langle \mathbf{S}_p^2 \rangle$ almost equal to 0, which indicates only a slight breaking of the 2α core. However, as seen in the large $\langle \mathbf{S}_p^2 \rangle$ values in the 2_2^+ and 5_1^- states, the 2α core structures dissociate in these band terminal states of the $K^\pi = 0_2^+$ and 1^- bands. Especially, the total spin $J = 2$ in the 2_2^+ state is composed of the aligned total-angular momentum of the p -shell protons, because the state has a neutron p -shell closure which gives no contribution to the total spin. We find that the non-zero intrinsic-spin components in these states are sensitive to the strength of the spin-orbit force. On the other hand, the 1_2^+ state has a quite different structure from that of the 2α -core state. It is a spin-aligned state with proton spin, $\mathbf{S}_p \sim 1$, where one of the 2α clusters is completely broken. In fact, no dumbbell shape is seen in the proton density of this state (Fig. 4). The alignment of the intrinsic spins is the origin of the unnatural spin parity of this state. This 1_2^+ state is analogous to the $3/2^-$ state at 8.4 MeV in ^{11}Be , and also to the 1_1^+ state in ^{12}C , in which cluster breaking occurs due to the aligned intrinsic spins.

The deformation parameter (β) of the proton density shown in Fig. 4 is a useful quantity in order to quantitatively discuss the developments of clustering in the 2α core states. Here, we explain the cluster developments in relation to the neutron structure, such as the neutron deformation and neutron intrinsic spin.

In the $K^\pi = 0_1^+$ band, the states have a prolate deformation with the developed 2α core, as shown in Fig. 4. In the $0_1^+, 2_1^+$ and 4_1^+ states, the 2α core well develops following prolate deformation of the neutron density, which is caused by the 2 neutrons in a longitudinal sd -orbit. The non-zero total intrinsic spin of neutrons of the ground state shown in Table.V is considered to come from a sub-shell closure effect of the neutron $p_{3/2}$ -shell. As the total spin increases, the alignment of the intrinsic spins of the sd -shell neutrons increases (Table.V), and the neutron deformation becomes small in the high-spin region, $J \geq 6$. As a result, the clustering become weak in the 6_1^+ and 8_1^+ states, as found in the reduction of the proton deformation parameter (Fig. 4).

In the $K^\pi = 0_2^+$ band with the dominant $0\hbar\omega$ configurations, the neutron deformation is smaller than that in the $K^\pi = 0_1^+$ band. In the 0_2^+ state, 4 neutron pairs make a small tetrahedron-shape structure, which is approximately equivalent to the p -shell closed structure. Because of the shell effect of the neutron p -shell closure, the clustering is smaller than that in the 0_1^+ state.

In the $K^\pi = 0_3^+$ band, the 0_3^+ and 2_4^+ states have extremely developed cluster structures, like ${}^6\text{He}+{}^6\text{He}$. One of the reasons for the development of clustering is considered to be the orthogonality condition to the 0_1^+ and 2_1^+ states in the lower band. The inter-cluster distance shrinks with increasing total spin, due to the spin alignment. In the $0_3^+, 2_4^+$ and 4_2^+ , low matter density regions between the clusters are found (Fig. 4), while they disappear in the 6_2^+ and 8_1^+ states. The intrinsic structure changes for $K^\pi = 0_3^+$ rather rapidly with an increase of the total spin, as can be seen in the decrease of the deformation parameter (β), shown in Fig. 4 and also in the spin alignment of the neutron intrinsic spins (Table V).

In spite of the mixing of the states and the spin alignments, all of the states in the $K^\pi = 0_1^+, 0_3^+$ and 2_1^+ bands are dominated by $2\hbar\omega$ configurations with 2 neutrons in the sd -shell. It is another interesting problem to search for the weak-coupling cluster structure, which is described by the relative motion between the $2\text{-}{}^6\text{He}$ clusters. In pioneering work by M. Ito et al. [15], weak coupling states with $2\text{-}{}^6\text{He}$ clusters in ^{12}Be were studied. Although the calculation was not fully microscopic, because they did not make antisymmetrization of the neutrons between clusters, it is interesting that He-cluster states were suggested to appear near and above the threshold energies. The presently predicted 0_3^+ state is a candidate of the weak coupling cluster state, because of the large relative distance between clusters. However, in the 4_2^+ and 6_2^+ states in the $K^\pi = 0_3^+$ bands, the components of the weak coupling cluster state may not be large, since the He-cluster structure becomes weak due to the spin alignments. Instead, it is expected

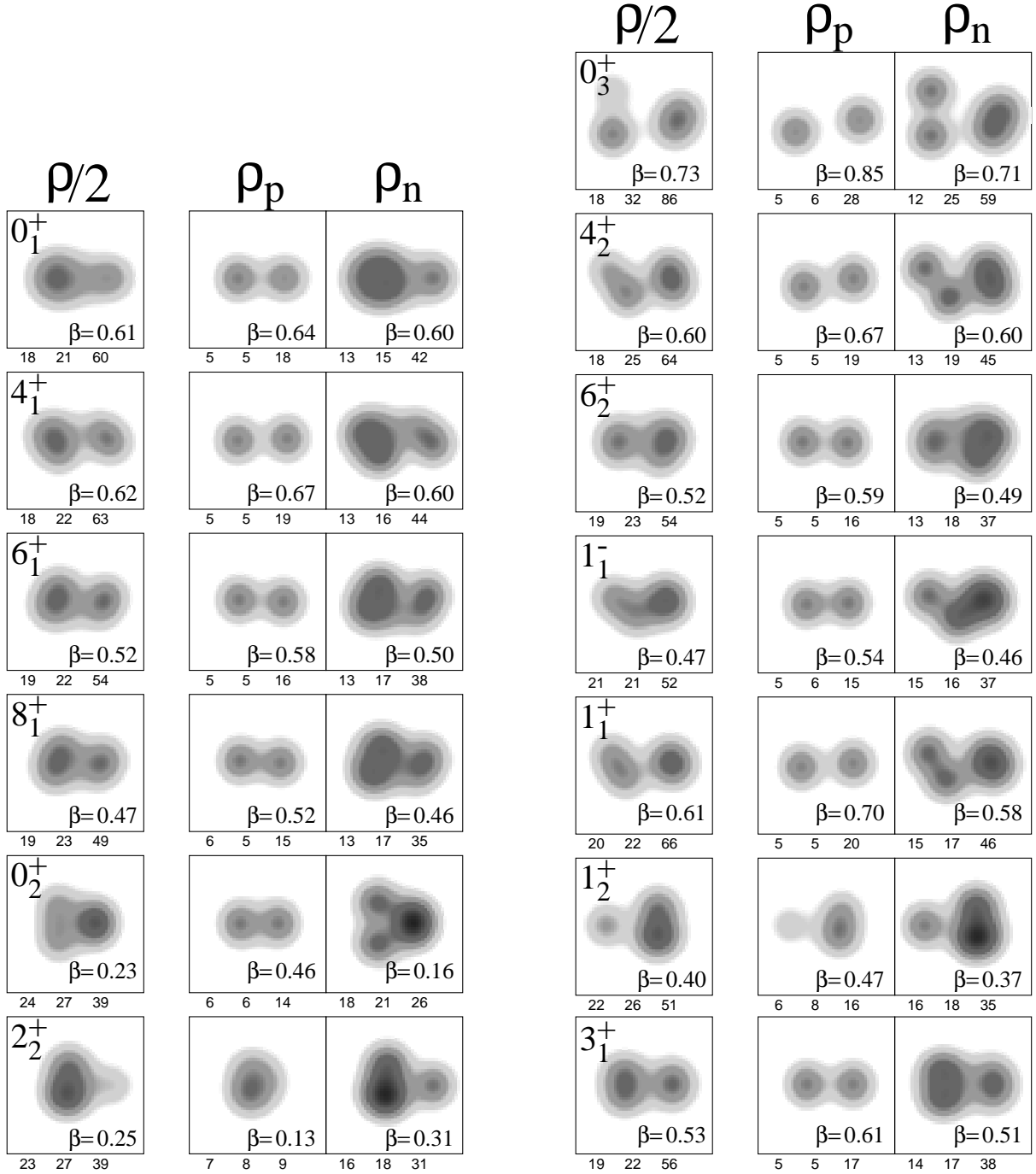


FIG. 4. Density distribution of the intrinsic state $\Phi_{AMD}(\mathbf{Z}_n^{J^\pm})$ before projection and diagonalization. The intrinsic system is projected onto a plane which contains the approximately longitudinal axis of the intrinsic state. The density is integrated along a transverse axis perpendicular to the plane. The densities for matter, protons and neutrons are presented at the left, middle and right, respectively. The expectation values of xx , yy , zz (the deformation parameters β) for the matter, proton and neutron densities are written below (at the bottom of) the figures. The size of the frame box is $10 \text{ fm} \times 10 \text{ fm}$.

that the molecular resonances with a weak-coupling cluster structure may exist above those spin-aligned states. We performed a simple VAP calculation of the higher states, and found that candidates of the weak-coupling states appear above those spin-aligned states with $2\hbar\omega$ configurations obtained in the present calculations. We find a 4_3^+ state with a developed ${}^6\text{He}+{}^6\text{He}$ -cluster structure at a 0.6 MeV higher energy than the 4_2^+ state. Although the 6_3^+ state was unstable for cluster escaping in the present VAP calculations using $m = 0.65$, we obtained a 6_3^+ state with a developed ${}^6\text{He}+{}^6\text{He}$ structure at a few MeV higher energy than the 6_2^+ state by using $m = 0.62$. Such weakly bound states should be carefully investigated by taking care of the threshold energies and the stability for particle decays.

Here, we stress that it is essential to consider the orthogonality to the lower states as well as antisymmetrization of all the nucleons in a study of the excited states of ${}^{12}\text{Be}$, because the present results suggest the existence of many 2α core states in the low-energy region. Although these states are not necessarily written in terms of ${}^6\text{He}+{}^6\text{He}$ clusters, such lower states must have effects on the higher weak-coupling cluster states.

The negative-parity states 1_1^- , 2_1^- , 3_1^- , 4_1^- and 5_1^- in the $K^\pi = 1_1^-$ band are deformed states with cluster structures. The deformed structures of the neutron density are made from the dominant $1\hbar\omega$ excited configurations with one neutron in the sd -shell. The neutron prolate deformation in this band is smaller than the states in the $K^\pi = 0_1^+$ band. The smaller neutron deformation effects the weaker cluster development in the $K^\pi = 1_1^-$ band compared with those in the $K^\pi = 0_1^+$ band. The 1_1^- , 2_1^- , 3_1^- , 4_1^- states have axially asymmetric neutron structures, while the band terminal 5_1^- state has an approximately axially symmetric neutron density.

Next, we discuss the structures of the unnatural spin-parity states. As mentioned above, the unnatural spin-parity of the 1_2^+ state is caused by the aligned intrinsic spins of protons. On the other hand, the unnatural spin-parity of the other states (3_1^+ , 5_1^+ , 7_1^+ , 1_1^- and 0_1^-) originates from the aligned intrinsic spins of the sd -shell neutrons. Alignments of the neutron intrinsic spins were found in the 2_3^+ , 3_1^+ and 5_1^+ states, as seen in the expectation values of the squared total neutron spins, $\langle \mathbf{S}_n^2 \rangle \sim 2$, presented in Table V. The spin alignment is mainly caused by 2 sd -shell neutrons. The deformation and the density distribution of the intrinsic state of the 7_1^+ state are very similar to those of the 3_1^+ and 5_1^+ , though $\langle \mathbf{S}_n^2 \rangle$ in the 7_1^+ state is slightly smaller. The 1_1^+ and 0_1^- states with unnatural spin-parity have aligned intrinsic spins of neutrons, like the states in the $K^\pi = 2_1^+$ band. Although a ${}^6\text{He}+{}^6\text{He}$ -like structure is found in the 1_1^+ state, one of the ${}^6\text{He}$ clusters is an excited ${}^6\text{He}$ with $S_n = 1$ components.

The present results indicate the importance of treating degrees of freedom of the intrinsic spins for all the nucleons in a study of ${}^{12}\text{Be}$. The reasons can be summarized as follows. First of all, a closed $p_{3/2}$ -shell of neutrons plays an important role for the energy gain of the intruder ground state. Secondly, the alignments of intrinsic spins as $S = 1$ are necessary to describe the unnatural spin-parity states. In the third point, the spin alignment of the neutron intrinsic spins occurs in high spin states.

C. Picture of molecular orbits

As mentioned in the previous subsection, the 2α core structure appears in many of the states. The development of clustering is sensitive to the prolate deformation of the neutron density. We inspected the neutron structure based on the single-particle behavior of the valence neutrons surrounding the 2α core. We also considered the relation between the neutron orbits and the cluster development. We analyzed the the single-particle wave functions of the valence neutrons in the intrinsic states. The detailed formulation of how to extract the single-particle energies and wave functions from an AMD wave function is described in Refs. [5,7].

According to the picture of the single-particle orbits, the 2α core is composed of nucleons occupying the lowest 4 proton orbits and 4 neutron orbits. The higher 4 neutron orbits correspond to those of the valence neutrons surrounding the 2α core. By extracting the positive and negative components in the orbits, many of the single-particle orbits are found to be approximately parity-eigen states, as the amplitude of the dominant parity-eigen state is more than 70% in each orbit. Since the negative and positive-parity orbits of the valence neutrons are associated with the p -orbits and sd -orbits, respectively, we can classify the ground and excited states of ${}^{12}\text{Be}$ in terms of the $n\hbar\omega$ excitation, where n is the number of the valence neutrons with the dominant positive-parity components. The $K^\pi = 0_2^+$ band is approximately described by $0\hbar\omega$ configurations, while the $K^\pi = 0_1^+$, 0_3^+ , 2_1^+ bands are dominated by $2\hbar\omega$ configurations with 2 neutrons in sd -like orbits. On the other hand, the main components of the $K^\pi = 1_1^-$ band are $1\hbar\omega$ configurations.

The idea of molecular orbits surrounding a 2α core is helpful to understand the roles of the valence neutrons in neutron-rich Be isotopes. The molecular orbits in Be isotopes were suggested in a study of ${}^9\text{Be}$ with a $2\alpha + n$ cluster model [20]. They assumed σ -orbits and π -orbits which are made from linear combinations of the p -orbits around the α cores (see Fig.5). This idea was applied to neutron-rich Be isotopes by Seya et al. a long time ago [1]. In the 1990's von Oertzen et al. [3,27] revived this kind of research to understand the rotational bands of neutron-rich Be isotopes, and Itagaki et al. [8,9] described the structures of the low-lying states of ${}^{10}\text{Be}$ and ${}^{12}\text{Be}$ by assuming 2α core and

TABLE V. Total intrinsic spins of protons and neutrons in the spin-parity projected states $P_{MK'}^{J\pm}\Phi_{AMD}(\mathbf{Z}_{n_i}^{J_i\pi_i})$ before the diagonalization. The values J_i , π_i and n_i for the J_n^\pm states are listed in Table IV.

states	Total intrinsic spins	
	protons $\langle \mathbf{S}_p^2 \rangle$	neutrons $\langle \mathbf{S}_n^2 \rangle$
0_1^+	0.1	1.0
2_1^+	0.1	1.1
4_1^+	0.1	1.2
6_1^+	0.0	1.5
8_1^+	0.1	1.6
0_2^+	0.2	0.1
2_2^+	0.9	0.1
0_3^+	0.0	0.5
2_4^+	0.0	1.0
4_2^+	0.0	1.0
6_2^+	0.0	1.2
1_1^-	0.1	0.8
2_1^-	0.1	0.8
3_1^-	0.1	1.0
4_1^-	0.1	1.1
5_1^-	0.5	1.2
2_3^+	0.0	2.1
3_1^+	0.0	2.1
5_1^+	0.0	2.0
7_1^+	0.0	1.2
0_1^-	0.1	1.7
1_1^+	0.0	1.3
1_2^+	1.9	0.3
6_1^-	0.0	2.0

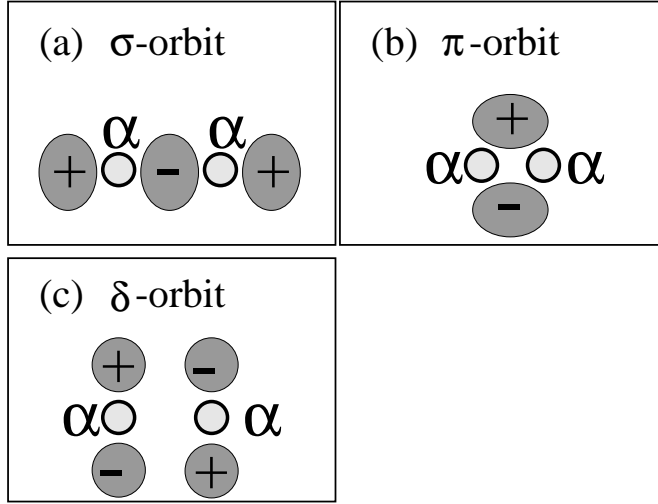


FIG. 5. Sketches for the molecular orbitals, (a) σ -orbitals, (b) π -orbitals, and (c) δ -orbitals surrounding 2α core. These molecular orbitals are explained by linear combinations of the p -shell orbitals around the α cores.

valence neutrons in the molecular orbitals. The formation of the 2α and valence neutron structures in neutron-rich Be isotopes was first guaranteed theoretically by the AMD calculation [2,5,6,7,11], where the existence of any clusters or molecular orbitals was not assumed. In these AMD studies, the viewpoint of the molecular orbit was found to be useful to understand the cluster development in ^{10}Be and ^{11}Be . Therefore, it is an interesting problem whether the states of ^{12}Be can be described by the molecular orbitals.

In the present results for ^{12}Be , we find a new kind of molecular orbit besides the suggested π -orbit and σ -orbit. In the positive-parity orbits of the valence neutrons in ^{12}Be , two kinds of molecular orbitals appear, both of which are associated with sd -orbitals. The first one is the σ -orbit (Fig. 5a), while the second one is a quite new molecular orbit, shown in Fig. 5c. This orbit is the other positive-parity orbit made from a linear combination of the p -orbitals around the α cores. As shown in Fig. 5c, the combined p -orbitals in this orbit are perpendicular to those in the σ -orbit. We call this new positive-parity orbit a δ -orbit in the present paper, although it is perpendicular to the so-called δ -orbit in the field of the molecular physics. In the case of ^{12}Be , the negative-parity orbit of the neutron surrounding 2α does not necessarily correspond to the pure molecular π -orbit, because the $p_{3/2}$ -shell closure can not be described by simple π -orbitals. Therefore, in the following discussions, we concentrate on the positive-parity orbits of the valence neutrons associated with the molecular σ -orbitals and δ -orbitals.

Fig. 6 shows the density distributions of the single-particle wave functions of the first and second highest neutron orbits. In the low-spin cluster states, the positive-parity orbits of the valence neutrons can be well associated with the two types of the molecular orbitals (σ and δ). In the 0_1^+ state, two valence neutrons with up and down spins occupy the σ -like orbitals, which have 2 nodes along the longitudinal axis. In the 0_3^+ state, which is dominated by the other $2\hbar\omega$ configurations, the two neutrons occupy δ -like orbitals. It is very surprising that the developed ${}^6\text{He}+{}^6\text{He}$ cluster structure in the 0_3^+ state is understood by the new molecular δ -orbitals. It occurs when 2 deformed ${}^6\text{He}$ clusters are attached in parallel. In the 0_2^+ state, all of the 4 valence neutrons are in the negative-parity orbitals. Comparing the energies of the 0_3^+ state with those of the 0_1^+ and 0_2^+ states, the δ orbit is the highest among the molecular orbitals (σ , π and δ).

The molecular σ -orbit is one of the reasons for the deformed ground state of ^{12}Be with the $2\hbar\omega$ configurations, which is lower than the closed neutron-shell state. Since Be nuclei prefer prolate deformations because of the 2α -cluster core, the σ -orbit gains kinetic energy in the developed cluster system. In pioneering studies, [9,11], the importance of the σ -orbit in the ground states of ^{11}Be and ^{12}Be were discussed in relation to a vanishing of the magic number. Thus, the neutrons in the σ -orbit play an important role in the cluster development of the ground state of ^{12}Be . On the other hand, in case of the 0_3^+ state, we consider that the cluster development is further enhanced due to the effect of the orthogonal condition to the 0_1^+ state.

The next problem is whether or not the molecular orbitals appear in the unnatural spin-parity 3_1^+ state, which has another deformed structure dominated by the $2\hbar\omega$ configuration. According to an analysis of single-particle wave functions, as shown in Fig. 6, we find that the positive-parity orbitals of the 3_1^+ state consist of a σ -like orbit and a δ -like orbit. As mentioned before, the total intrinsic spin of neutrons equals to that in the 3_1^+ state (see Table V). This means that the intrinsic spins of two neutrons in the σ -orbit and the δ -orbit are aligned to be one. It is a unique character of the 3_1^+ state to be different from the other $2\hbar\omega$ bands where the intrinsic spins of two neutrons in the

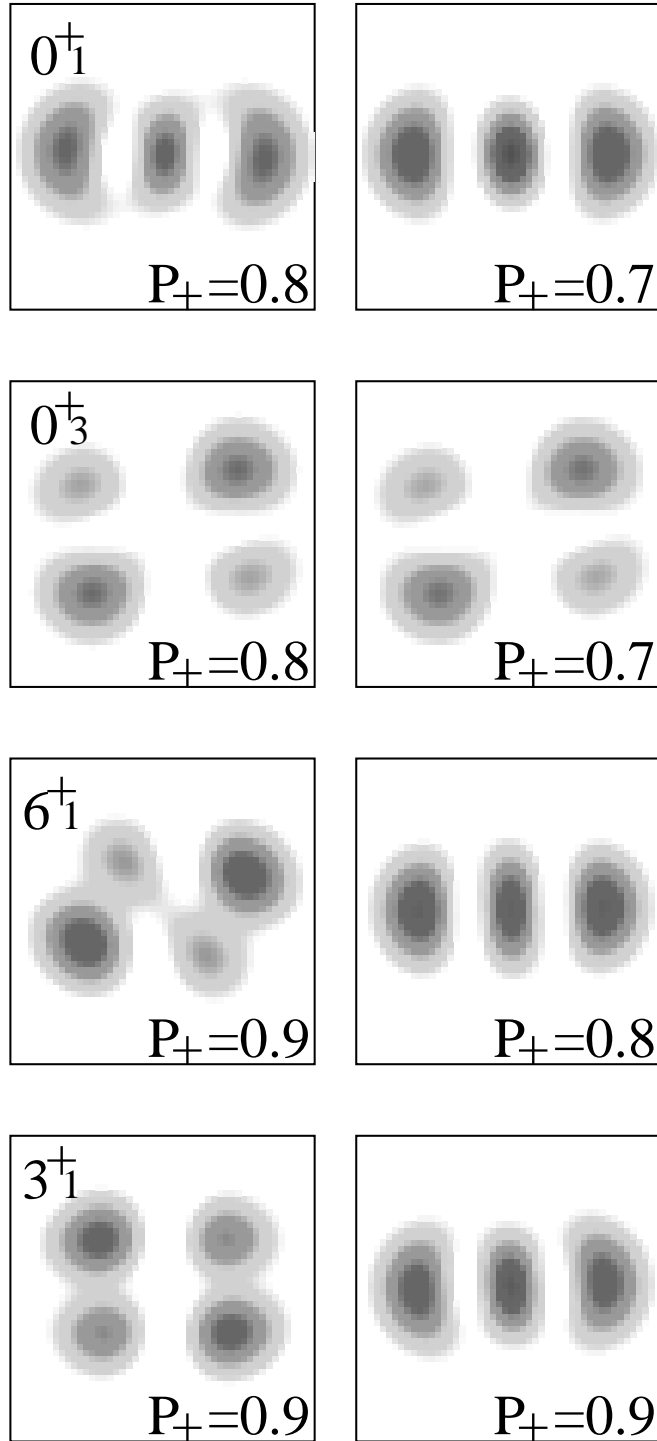


FIG. 6. Density distributions of the single-particle wave functions of the valence neutrons in the intrinsic wave functions of the 0_1^+ , 0_3^+ , 6_1^+ and 3_1^+ states. The figures at the left(right) show the densities regarding the positive-parity components of the first(second) highest neutron orbits. The value P_+ in each orbit indicates the squared amplitude of the contained positive-parity component.

same spatial positive-parity orbits couple off to be zero.

As mentioned above, in the case of the low-spin states in the deformed band, the highest two positive-parity orbits of the valence neutrons can be well associated with the σ and δ -orbits. However the positive-parity orbits in the high-spin states can not be classified by the simple σ and δ -orbits, but are related to the mixed orbits of the two. For example, the highest neutron orbit in the 6_1^+ states indicates the mixing of σ and δ , as shown in Fig. 6. As the total spin increases from 0_1^+ to 6_1^+ in the $K^\pi = 0_1^+$ band, the alignment of the neutron intrinsic spins grows accompanying mixing the δ -orbit in the σ -orbit.

The states in the negative-parity band ($K^\pi = 1_1^-$) are described by $1\hbar\omega$ configurations, because one of the highest 2 orbits is dominated by the positive-parity component, while the other one is almost a negative-parity orbit. The interesting point is that the 30% mixing of the positive-parity component in the negative-parity orbit gives rise to the axial asymmetric shape of the intrinsic state, as shown by the neutron density (Fig. 4).

In an analysis of ^{12}Be with the molecular orbits, it should be stressed that all of the states with a 2α core can not be necessarily described by pure molecular orbits: π , σ and δ -orbits. Firstly, the single-particle orbits of the valence neutrons are not parity-eigen orbits. For example, although the highest two neutron orbits in the 0_1^+ state are dominated by positive-parity components, they contain 20%~30% mixing of negative-parity contamination, which can not be regarded as the π -orbits but includes higher-shell configurations. Moreover, mixing of the σ and δ -orbits is found in the high-spin states in the $K^\pi = 0_1^+$ and $K^\pi = 0_3^+$ bands, as can be seen in the highest single-particle orbits of the 6_1^+ state (Fig. 6).

D. Systematics of the 2α clustering in Be isotopes

When we roughly regard the valence neutron orbits in the 0_1^+ , 1_1^- , 0_2^+ states of ^{12}Be as the π -orbits and the σ -orbits, these ^{12}Be states remind us of analogous states in ^9Be , ^{10}Be and ^{11}Be . In terms of the molecular orbits surrounding the 2α core, the typical rotational bands in these Be isotopes are classified by the number of occupied σ -orbits. Here, we use the notation $\pi^m\sigma^n$ for those states having m neutrons in the π -orbits and n neutrons in the σ -orbits around a 2α core. The valence neutron orbits in the lowest natural parity states ($^9\text{Be}(1/2^-)$, $^{10}\text{Be}(0_1^+)$, $^{11}\text{Be}(1/2^-)$ and $^{12}\text{Be}(0_2^+)$) are described as $\pi^m\sigma^0$, and those in the lowest unnatural parity states ($^9\text{Be}(1/2^+)$, $^{10}\text{Be}(1^-)$, $^{11}\text{Be}(1/2^+)$ and $^{12}\text{Be}(1^-)$) are noted as $\pi^{m-1}\sigma^1$, while the $^{10}\text{Be}(0_2^+)$, $^{11}\text{Be}(3/2_-^-)$ and $^{12}\text{Be}(0_1^+)$ states correspond to $\pi^{m-2}\sigma^2$, where m is the number of valence neutrons around the 2α core (see also Refs. [3,7,11,20]). It is important that the number of neutrons in the σ -orbits influences the spatial development of the 2α core. The changes in the relative distance between the 2 α clusters in the Be isotopes are shown in Fig. 7. The dotted, thick solid and thin solid lines correspond to the distances in the band head states with zero ($\pi^m\sigma^0$), one ($\pi^{m-1}\sigma^1$) and two ($\pi^{m-2}\sigma^2$) neutrons in the σ -orbit. In each Be isotope, the 2α distance is smallest in the σ^0 state and becomes larger and larger with increasing number of the occupied σ -orbits, because of the energy gain of the σ -orbits in the developed cluster system. Comparing the 2α distance in each line, the dependence on the neutron number shows that the cluster development systematically decreases as the number of the occupied π -orbits increases. Especially, a drastic change in the σ^0 states from ^9Be to ^{10}Be is caused by the $p_{3/2}$ sub-shell closure effect. Also, in the σ^1 and σ^2 lines, there exist gaps between the states with a closed $p_{3/2}$ -shell and those with an open $p_{3/2}$ -shell. Thus, the closed $p_{3/2}$ -shell plays an important role in weakening the 2α development.

One of the interesting features of neutron-rich Be isotopes is vanishing of the neutron magic number $N = 8$ in ^{11}Be and ^{12}Be . In Fig. 7, the ground states are plotted as open circles. The intruder ground states in ^{11}Be and ^{12}Be correspond to points on the σ^1 and σ^2 lines, respectively. As shown in the Fig. 7, the 2α distances in the ground state of ^{11}Be and ^{12}Be are about 3 fm. We may conjecture that the magnitude of 3 fm is the natural distance between 2 α , which is energetically favored in these neutron-rich Be isotopes. Therefore, one of the reasons for the intruder ground states can be understood to be a restoration of the natural distance at about 3 fm in the very neutron-rich Be isotopes.

The $N = 6$ sub-shell closure effects are clearly seen in the energy gaps of 6 MeV as well as in the drastic structure changes between the σ^0 and σ^1 states in ^{10}Be . The sub-shell effect is also reflected in the structure change between the σ^1 and σ^2 states in ^{11}Be , as shown in the 2α distance. This means that we can regard the vanishing of the magic number in neutron-rich Be isotopes as a shift of the neutron magic number from $N = 8$ to $N = 6$.

E. Inter-cluster motion and He decay width

In order to investigate the inter-cluster motion, we extracted the relative wave functions between clusters in the $^6\text{He}+^6\text{He}$ and $^8\text{He}+^4\text{He}$ channels. We assumed that the intrinsic wave functions of the He clusters are given by the

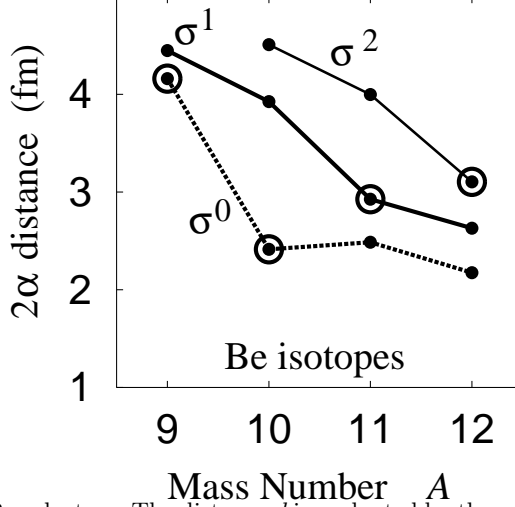


FIG. 7. Relative distance between 2- α clusters. The distance d is evaluated by the relative distance between the mean centers of 2 proton pairs, defined as $d \equiv \sqrt{(\text{Re}[\mathbf{Z}_1 + \mathbf{Z}_2 - \mathbf{Z}_3 - \mathbf{Z}_4])^2 / 2\sqrt{v}}$. The dotted, thick solid and thin solid lines correspond to the distances in the band head states with zero (σ^0), one (σ^1) and two (σ^2) neutrons in the σ orbits. Namely, the lines (σ^0, σ^1 and σ^2) correspond to $\{^9\text{Be}(1/2_1^-), ^{10}\text{Be}(0_1^+), ^{11}\text{Be}(1/2_1^-), ^{12}\text{Be}(0_2^+)\}$, $\{^9\text{Be}(1/2_1^+), ^{10}\text{Be}(1_1^-), ^{11}\text{Be}(1/2_1^+), ^{12}\text{Be}(1_1^-)\}$ and $\{^{10}\text{Be}(0_2^+), ^{11}\text{Be}(3/2_2^-), ^{12}\text{Be}(0_1^+)\}$, respectively. The open circles indicate the ground states.

0^+ states of ^4He , ^6He , ^8He in the SU_3 limit with the same width parameter as that of ^{12}Be . The detailed structures of the ^6He nucleus, such as the neutron halo, are omitted in the present analysis for simplicity. We estimated the inter-cluster relative motions in ^{12}Be by the relative wave functions ($\tilde{u}_L(r)$), which were calculated by projecting the ^{12}Be wave functions to the cluster model space expressed by the superpositions of Brink functions. The cluster probability was estimated by $\int r^2 \tilde{u}_L^2(r) dr = \tilde{S}_u$. The detailed definitions and the practical calculation of $\tilde{u}_L(r)$ and \tilde{S}_u are explained in appendix A. $\tilde{u}_L(r)$ and \tilde{S}_u correspond to the reduced width amplitude, $y_L(r)$, and the spectroscopic factors, S , respectively. Especially, $\tilde{u}_L(a)$ should equal to $y_L(a)$ in the outer region, where the effect of the inter-cluster antisymmetrization disappears.

Figs. 8 and 9 show the relative wave functions ($r\tilde{u}_L(r)$) in the $^6\text{He}+^6\text{He}$ and $^8\text{He}+^4\text{He}$ channels extracted from the obtained $J = L$ states of ^{12}Be , respectively. The amplitudes $r\tilde{u}_L(r)$ at the channel radius $a = 5$ fm and the cluster probabilities (\tilde{S}_u) are presented in Table VI.

In both the cluster channels, the amplitude $|r\tilde{u}_L(r)|$ is larger in the low-spin states compared with the high-spin states. In each band, the amplitude becomes small with an increase of the spin, because the spin alignments in the high spin states reduce the overlap with the $\text{He}(0^+)$ components. In particular, the amplitudes in the $J = 8$ state are very small.

In the $^6\text{He}+^6\text{He}$ channel, the amplitude at the surface region about 5 fm is largest in the 0_3^+ state. It indicates the spatially developed ^6He cluster in the state. Compared with that in the 0_3^+ state, the amplitude shifts inward in the 0_1^+ state. Since the 0_2^+ state has no developed clustering, the surface amplitude is smallest. The significant amplitudes $|r\tilde{u}_L(r)|$ at about 4 fm in the 0_2^+ state are caused by mixing with the 0_1^+ state. With respect to the $J^\pm = 2^+, 4^+$, and 6^+ states, the surface amplitudes $|au_L(a)|(a = 5 \text{ fm})$ are larger in the $K^\pi = 0_3^+$ band than in the $K^\pi = 0_1^+$ band, as in the case of the 0^+ states. This means that the development of $^6\text{He}+^6\text{He}$ clustering is more remarkable in the $K^\pi = 0_3^+$ band. On the other hand, in the $^4\text{He}+^8\text{He}$ channel, the states in the $K^\pi = 0_1^+$ band have larger amplitudes in the region $3 \leq r \leq 4$ fm, compared with those in the $K^\pi = 0_3^+$ band. We conclude that the $K^\pi = 0_1^+$ band has both components of $^6\text{He}+^6\text{He}$ and $^4\text{He}+^8\text{He}$ cluster structures, while in the $K^\pi = 0_3^+$ band, the $^6\text{He}+^6\text{He}$ clustering appears predominantly. These results strongly suggested that the neutrons around the 2α core move about over the whole system in the $K^\pi = 0_1^+$ band states, while in the $K^\pi = 0_3^+$ band states they move about not over the whole system, but around either of the two α clusters.

We next mention the partial decay widths of the excited states above the threshold energies of the He decays. We calculated the theoretical values of the partial decay widths ($\Gamma_{4\text{He}}$ and $\Gamma_{6\text{He}}$) concerning the simple binary decays, $^6\text{He}(0^+)+^6\text{He}(0^+)$ and $^8\text{He}(0^+)+^4\text{He}(0^+)$, using the method of reduced width amplitudes:

$$\Gamma_{4,6\text{He}} = 2P_L(a) \cdot \gamma_{8,6\text{He}}^2(a), \quad (13)$$

$$P_L(a) = \frac{ka}{F_L^2(ka) + G_L^2(ka)}, \quad (14)$$

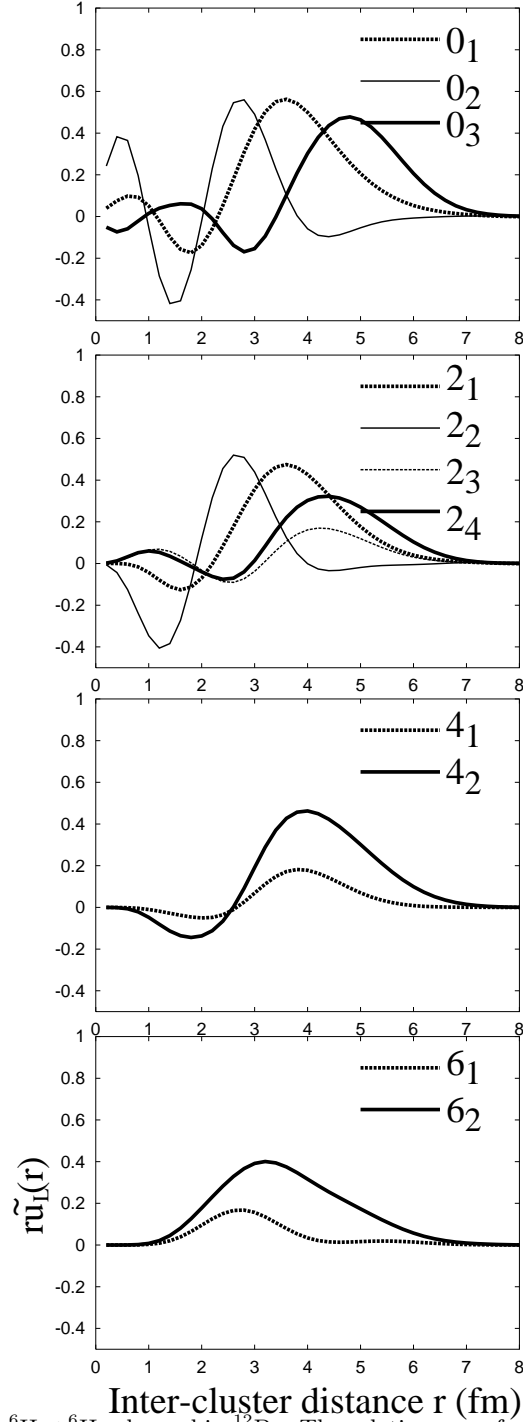


FIG. 8. Inter-cluster motion in the ${}^6\text{He}+{}^6\text{He}$ channel in ${}^{12}\text{Be}$. The relative wave function ($r\tilde{u}_L(r)$) is defined in the text and the appendix. The thick solid(dashed) lines are $r\tilde{u}_L(r)$ of the states in the $K^\pi = 0_3^+$ ($K^\pi = 0_1^+$) band.

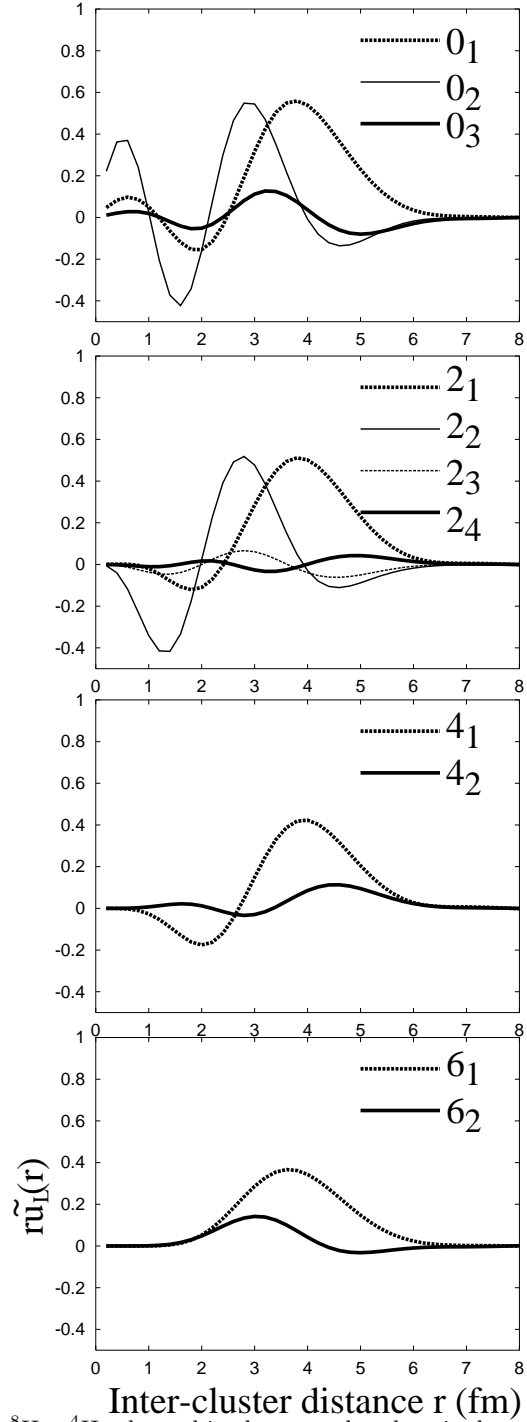


FIG. 9. Inter-cluster motion in the ${}^8\text{He}+{}^4\text{He}$ channel in the ground and excited states of ${}^{12}\text{Be}$. The wave function $r\tilde{u}_L(r)$ is defined in the text and the appendix.

TABLE VI. Theoretical results of the cluster probability of the He cluster channels in ^{12}Be . The magnitudes $|a\tilde{u}_L(a)|$ of the relative wave functions between clusters at the surface $a = 5$ fm are also shown.

J_n^+	${}^6\text{He}+{}^6\text{He}$	\tilde{S}_u	${}^8\text{He}+{}^4\text{He}$	${}^6\text{He}+{}^6\text{He}$	$ a\tilde{u}_L(a) $	$\text{fm}^{-1/2}$ ${}^8\text{He}+{}^4\text{He}$
0_1^+	0.49		0.47	0.21		0.23
0_2^+	0.44		0.46	0.05		0.11
0_3^+	0.37		0.02	0.46		0.08
2_1^+	0.35		0.40	0.18		0.23
2_2^+	0.36		0.38	0.02		0.09
2_3^+	0.05		0.01	0.12		0.05
2_4^+	0.18		0.003	0.27		0.04
4_1^+	0.04		0.28	0.07		0.21
4_2^+	0.38		0.02	0.30		0.09
6_1^+	0.04		0.22	0.02		0.15
6_2^+	0.32		0.03	0.17		0.03
8_1^+	0.0002		0.03	0.002		0.09

TABLE VII. The theoretical partial decay widths for the ${}^6\text{He}+{}^6\text{He}$ and ${}^8\text{He}+{}^4\text{He}$ decays. The channel radius is chosen to be $a = 5$ fm. The square of the relative wave functions $|a\tilde{u}_L^G(a)|^2$ ($L = J$) at the channel radius are also listed.

J_n^+	$ a\tilde{u}_L^G(a) ^2$	$\Gamma_{{}^6\text{He}}$ (keV)	$ a\tilde{u}_L^G(a) ^2$	$\Gamma_{{}^4\text{He}}$ (keV)
0_3^+	2.1×10^{-1}	8×10^2	6.4×10^{-3}	5×10^1
2_4^+	7.3×10^{-2}	2	1.8×10^{-3}	3
4_2^+	9.1×10^{-2}	7	9.0×10^{-3}	5
6_2^+	3.0×10^{-2}	16	1.0×10^{-3}	1
8_1^+	1×10^{-5}		8.2×10^{-3}	1

$$\gamma_{8,6\text{He}}^2(a) = \frac{\hbar^2}{2\mu a} |ay_L(a)|^2, \quad (15)$$

$$(16)$$

where k is the wave number of the resonance energy (E^r), $k = \sqrt{2\mu E^r/\hbar^2}$, a is the channel radius, and F_L and G_L are the regular and irregular Coulomb functions. The resonance energies were evaluated by subtracting the experimental threshold energies of the channels from the theoretical excitation energies. In the present calculations, the amplitudes $|ay_L(a)|$ were approximated by $|r\tilde{u}_L(r)|(r = a)$. In practical calculations of the decay widths, we modified the original $r\tilde{u}_L(r)$ so as to smoothly connect with the irregular Coulomb function ($G_L(kr)$) at the surface region. The points to smoothly connect $r\tilde{u}_L(r)$ with $G_L(kr)$ are found to be at around $r = 5$ fm in most of the resonance states.

In Table VII, the theoretical values of the square of the modified amplitudes and the partial decay widths are listed. The channel radius (a) is chosen to be 5 fm. The width of the 0_3^+ state for the ${}^6\text{He}$ decay is broad because of the developed ${}^6\text{He}+{}^6\text{He}$ cluster structure and the lack of a centrifugal barrier. Although the excited states seem to be stable for the partial decay width of the He channels, the stability of the resonance states should be carefully investigated by taking all of the other possible decay channels, such as the neutron decays and the excited He decays, into account.

VI. SUMMARY

We studied the structures of the ground and excited states of ^{12}Be based on the framework of the AMD method. This was the first microscopic calculation which systematically reproduced the energy levels of all of the spin-assigned states in ^{12}Be , except for the 1^- state. One of the present discoveries is the $K^\pi = 0_3^+$ band with the ${}^6\text{He}+{}^6\text{He}$ cluster structure, which corresponds well to the states recently observed in the He-He break-up reactions. The ground-state properties, such as the β -decay strength and the $E1$ transition strength, were reproduced by the present calculations,

which suggest that the ground state is dominated by a deformed intruder state with the developed cluster structure. The theoretical results predicted many low-lying excited states. It was found that most of them have a 2α core, while the 1_2^+ state has a no α -cluster structure.

We analyzed the structures and the single-particle wave functions of the intrinsic states, and found rotational bands with $K^\pi = 0_1^+, 0_2^+, 1_1^-, 0_3^+, 2_1^+$, which are dominated by the $2\hbar\omega, 0\hbar\omega, 1\hbar\omega, 2\hbar\omega$ and $2\hbar\omega$ configurations, respectively. The $2\hbar\omega$ and $1\hbar\omega$ states have deformed structures with a 2α core. In the positive-parity orbits occupied by the valence neutrons, we found the molecular orbits, σ -orbits and the new δ -orbits. The positive-parity molecular orbits play an important role in the development of cluster structure. Especially, the reason for the intruder ground state can be understood by the energy gain of the σ -orbit in the developed cluster state. Although the molecular orbits are helpful to understand the structures of the band head states, the model of the 2α and 4 neutrons in the molecular orbits is too simple to describe all of the excited states, because such phenomena as the intrinsic spin alignment, the dissociation or breaking of 2α core and the mixing of the molecular orbits appear in ^{12}Be .

We discussed the inter-cluster motions in the $^6\text{He}+^6\text{He}$ and $^8\text{He}+^4\text{He}$ channels, and estimated the partial width of these decay channels with the method of reduced width amplitudes. The analyzed results of the partial widths strongly suggest that the neutrons of the $K^\pi = 0_3^+$ band move around either of two α clusters, while the neutrons of the $K^\pi = 0_1^+$ band move over the whole system.

We also discussed the systematics of the cluster development in the neutron-rich Be isotopes according to the classification of the states with the number of neutrons in the σ -orbits. Concerning the vanishing of the neutron magic number $N = 8$ in the Be isotopes, we suggested that the reason for the intruder ground states may be explained by the restoration of the natural distance between the 2 α clusters.

ACKNOWLEDGMENTS

The authors would like to thank Dr. N. Itagaki for many discussions. They are also thankful to Prof. W. Von Oertzen for helpful comments. Valuable comments of Prof. S. Shimoura and Dr. A. Saito are also acknowledged. The computational calculations in this work were supported by the Supercomputer Project Nos. 58 and 70 of High Energy Accelerator Research Organization(KEK), and also supported by Research Center for Nuclear Physics in Osaka University and Yukawa Institute for Theoretical Physics in Kyoto University. This work was partly supported by Japan Society for the Promotion of Science and a Grant-in-Aid for Scientific Research of the Japan Ministry of Education, Science and Culture. This work was partially performed in the ‘‘Research Project for Study of Unstable Nuclei from Nuclear Cluster Aspects’’ sponsored by Institute of Physical and Chemical Research (RIKEN).

REFERENCES

-
- [1] M. Seya, M. Kohno, and S. Nagata, Prog. Theor. Phys. **65**, 204 (1981).
 - [2] Y. Kanada-En’yo, H. Horiuchi and A. Ono, Phys. Rev. C **52**, 628 (1995); Y. Kanada-En’yo and H. Horiuchi, Phys. Rev. C **52**, 647 (1995).
 - [3] W. von Oertzen, Z. Phys. A **354**, 37 (1996); **357**, 355(1997).
 - [4] K. Arai, Y. Ogawa, Y. Suzuki and K. Varga, Phys. Rev. C **54**, 132 (1996).
 - [5] A. Doté, H. Horiuchi, and Y. Kanada-En’yo, Phys. Rev. C **56**, 1844 (1997).
 - [6] Y. Kanada-En’yo, H. Horiuchi and A. Doté, J. Phys. G, Nucl. Part. Phys. **24** 1499 (1998).
 - [7] Y. Kanada-En’yo, H. Horiuchi and A. Doté, Phys. Rev. C **60**, 064304(1999).
 - [8] N. Itagaki and S. Okabe, Phys. Rev. C **61**, 044306 (2000);
 - [9] N. Itagaki, S. Okabe and K. Ikeda, Phys. Rev. C **62**, 034301 (2000).
 - [10] Y. Ogawa, K. Arai, Y. Suzuki, and K. Varga, Nucl. Phys. **A673** 122 (2000).
 - [11] Y. Kanada-En’yo and H. Horiuchi, Phys. Rev. C **66**, 024305(2002).
 - [12] A.A. Korshennikov, et al., Phys. Lett. **B** 343, 53(1995).
 - [13] M. Freer, et al., Phys. Rev. Lett. **82**, 1383 (1999); M. Freer, et al., Phys. Rev. C **63**, 034301 (2001).
 - [14] A. Saito, et al., Proc. Int. Sympo. on Clustering Aspects of Quantum Many-Body Systems, eds A. Ohnishi, N. Itagaki, Y. Kanada-En’yo and K. Kato, (World Scientific Publishing Co.).

- [15] M. Ito, Y. Sakuragi, Y. Hirabayashi, Phys.Rev.**C 63**, 064303(2001).
- [16] H. Iwasaki, et al. Phys.Lett.**B491**, 8(2000).
- [17] S. Shimoura, et al., preprint, CNS-REP-47(2002).
- [18] T. Suzuki and T. Otsuka, Phys. Rev. bf C 56, 847(1997).
- [19] Y. Kanada-En'yo, Phys. Rev. **C 66**, 011303(2002).
- [20] S. Okabe, Y. Abe, and H. Tanaka, Prog. Theory. Phys.**57**, 866(1977); S. Okabe, Y. Abe, Prog. Theory. Phys.**61**, 1049(1979).
- [21] Y. Kanada-En'yo and H. Horiuchi, Prog. Theor. Phys. **93**, 115 (1995).
- [22] Y. Kanada-En'yo, Phys. Rev. Lett. **81**, 5291 (1998).
- [23] T. Ando, K.Ikeda, and A. Tohsaki, Prog. Theor. Phys. **64**, 1608 (1980).
- [24] N. Yamaguchi, T. Kasahara, S. Nagata, and Y. Akaishi, Prog. Theor. Phys. **62**, 1018 (1979); R. Tamagaki, Prog. Theor. Phys. **39**, 91 (1968).
- [25] I. Tanihata et al., Phys.Lett.B 206, 592(1988).
- [26] W.-T. Chou, E. K. Warburton and B. A. Brown, Phys. Rev. **C47**, 163(1993).
- [27] W. von Oertzen, Nuovo Cimento 110, **895**, (1997).
- [28] Y. Kanada-En'yo and H. Horiuchi, Prog. Theor. Phys. Suppl.**142**, 205(2001).
- [29] H. Horiuchi, Chapter III of Suppl. of Prog. Theor. Phys. No.62(1977).

APPENDIX A: INTER CLUSTER WAVE FUNCTIONS

The calculational methods of the reduced width amplitudes(R.W.A.) and the inter-cluster wave functions concerning He(0^+) cluster decays are explained in this appendix.

1. Reduced width amplitudes and cluster model space

The reduced width amplitudes, $y_L(a)$, are defined as follows:

$$y_L(a) \equiv \frac{1}{\sqrt{1 + \delta_{C_1, C_2}}} \sqrt{\binom{A}{A_1}} \left\langle \frac{\delta(r-a)}{r^2} Y_{L0}(\hat{r}) \phi_0(C_1) \phi_0(C_2) | \Phi_L \right\rangle, \quad (\text{A1})$$

where Φ_L is the internal wave function of a model wave function and $\phi_0(C_1)$ and $\phi_0(C_2)$ are the internal wave functions of the clusters C_1 and C_2 . The mass numbers of the system and the clusters C_1 and C_2 are A , A_1 and A_2 , respectively.

Here, we briefly review the R.W.A. in the system of two clusters written in the form of RGM(resonating group method) or GCM(generator coordinate method) wave functions. The detailed calculational methods of the RGM and GCM kernels are described, for example, in Ref. [29]. We assume the same width parameter (ν) for clusters C_1 and C_2 described by harmonic oscillator shell model wave functions. When $\Phi_{LC_1C_2}$ is an RGM-type wave function, which is expressed as

$$\Phi_{LC_1C_2} = \frac{1}{\sqrt{(1 + \delta_{C_1, C_2}) \binom{A}{A_1}}} \mathcal{A}\{\chi_L(r) Y_{L0}(\hat{r}) \phi_0(C_1) \phi_0(C_2)\}, \quad (\text{A2})$$

the R.W.A. $y_L(a)$ can be calculated based on the knowledge of the RGM norm kernel as follows. By expanding the relative motion $\chi_L(r)$ with the radial harmonic oscillator (H.O.) wave functions $R_{nL}(r, \nu')$ with the width parameter $\nu' = \frac{A_1 A_2}{A} \nu$ as

$$\chi_L(r) = \sum_n e_{nL} R_{nL}(r, \nu'), \quad (\text{A3})$$

we obtain

$$y_L(a) = \sum_n e_{nL} \mu_{nL} R_{nL}(a, \nu'), \quad (\text{A4})$$

where μ_{nL} are the eigen values of the RGM norm kernel, defined as

$$\mu_{nL} \equiv \frac{1}{1 + \delta_{C_1, C_2}} \langle R_{nL}(r, \nu') Y_{L0}(\hat{r}) \phi_0(C_1) \phi_0(C_2) | \mathcal{A}\{R_{nL}(r, \nu') Y_{L0}(\hat{r}) \phi_0(C_1) \phi_0(C_2)\} \rangle. \quad (\text{A5})$$

If $\Phi_{LC_1C_2}$ is normalized to unity, $\langle \Phi_{LC_1C_2} | \Phi_{LC_1C_2} \rangle = 1$, the following equation is satisfied:

$$\sum_n e_{nL}^2 \mu_{nL} = 1. \quad (\text{A6})$$

The values μ_{nL} reflect the effect of the antisymmetrization between the clusters. In the case of n, L of the forbidden state, μ_{nL} equals to zero. With an increase of the quanta n , the antisymmetrization effect becomes smaller and μ_{nL} approaches unity.

In the case of general A-nucleon wave functions, Φ_L can be separated into the cluster part and the non-cluster part,

$$\Phi_L = \mathcal{A}\{\chi_L(r)Y_{L0}(\hat{r})\phi_0(C_1)\phi_0(C_2)\} + \Phi_L^R, \quad (\text{A7})$$

where Φ_L^R is the residual part after projection of the cluster model space, and satisfies $\langle Y_{L0}(\hat{r})\phi_0(C_1)\phi_0(C_2) | \Phi_L^R \rangle = 0$. In the same way as the RGM wave functions, the R.W.A. of Φ_L can be obtained with equation A4 by using an expansion of $\chi_L(r)$ with the H.O. functions shown in Eq.A3. The normal spectroscopic factors S are calculated as

$$S = \int y_L(r)^2 r^2 dr = \sum_n \mu_{nL}^2 e_{nL}^2. \quad (\text{A8})$$

It is useful to consider the relative wave function between clusters,

$$u_L(a) = \sum_n e_{nL} \mu_{nL}^{1/2} R_{nL}(a, \nu'), \quad (\text{A9})$$

because $|u_L(a)|^2$ can be interpreted as the probability density at relative distance a . The total probability of the clustering component in Φ_L is

$$S_u = \int u_L(r)^2 r^2 dr = \sum_n \mu_{nL} e_{nL}^2. \quad (\text{A10})$$

It is easily found that $S_u = 1$ for the RGM wave functions $\Phi_{LC_1C_2}$ from equation A6.

The R.W.A. of the wave function $\Psi_L(^{12}\text{Be})$ with the angular momentum L in the AMD framework are

$$y_L(a) \equiv \frac{1}{\sqrt{1 + \delta_{C_1, C_2}}} \sqrt{\binom{A}{A_1}} \langle \frac{\delta(r-a)}{r^2} Y_{L0}(\hat{r}) \phi_0(C_1) \phi_0(C_2) | \Phi_L(^{12}\text{Be}) \rangle, \quad (\text{A11})$$

where the center of mass motion ω_0 of the wave function $\Psi_L(^{12}\text{Be})$ is separated from the internal wave function as

$$\Psi_L(^{12}\text{Be}) = \omega_0(\mathbf{X}_G) \cdot \Phi_L(^{12}\text{Be}), \quad \omega_0(\mathbf{X}_G) \equiv \left(\frac{2A\nu}{\pi} \right)^{3/4} e^{-A\nu\mathbf{X}_G^2}, \quad \mathbf{X}_G \equiv \frac{1}{A} \sum_{i=1, A} \mathbf{r}_i, \quad (\text{A12})$$

and $\phi_0(C_n)$ ($C_n = ^4\text{He}, ^6\text{He}, ^8\text{He}$) are the intrinsic wave functions of the SU_3 -limit 0^+ states of the He clusters. In order to project to the cluster model space from the ^{12}Be wave functions ($\Phi_L(^{12}\text{Be})$) and calculate the radial wave functions ($\chi_L(r)$) between the clusters, as mentioned in Eq.A7, we use the orthonormal sets of the GCM wave functions. Concerning the k -th cluster wave functions $\Psi^c(\mathbf{b}_k)$ with the inter-cluster distances $\{b_k\}$, we adopt Brink-type functions, where two clusters, $C_1 = ^{A_1}\text{He}$ and $C_2 = ^{A_2}\text{He}$, written in the SU_3 limit representation are located at the points $(0, 0, \frac{A_2}{A_1+A_2}b_k)$ and $(0, 0, -\frac{A_1}{A_1+A_2}b_k)$, respectively,

$$\Psi^c(\mathbf{b}_k) = q_0 \mathcal{A}\{\Psi(C_1, \frac{A_2}{A} \mathbf{b}_k) \Psi(C_2, -\frac{A_1}{A} \mathbf{b}_k)\}, \quad \mathbf{b}_k = (0, 0, b_k). \quad (\text{A13})$$

The width parameters of the He clusters are chosen to be the same as that of the ^{12}Be wave functions for simplicity. Then we can rewrite $\Psi^c(\mathbf{b}_k)$ as

$$\Psi^c(\mathbf{b}_k) = \omega_0(\mathbf{X}_G) \cdot \Phi^c(\mathbf{b}_k), \quad (\text{A14})$$

$$\Phi^c(\mathbf{b}_k) = \frac{n_0}{\sqrt{(1+\delta_{C_1, C_2}) \binom{A}{A_1}}} \mathcal{A}\{\Gamma(\mathbf{r}, \mathbf{b}_k, \nu') \phi_0(C_1) \phi_0(C_2)\}, \quad (\text{A15})$$

$$\Gamma(\mathbf{r}, \mathbf{b}_k, \nu') = \left(\frac{2\nu'}{\pi} \right)^{3/4} e^{-\nu'(\mathbf{r}-\mathbf{b}_k)^2} \quad (\text{A16})$$

$$(\text{A17})$$

In each L , we make a set of the orthonormal basis $\tilde{\Phi}_{k,L}$ by linear combinations of the total-spin-projected GCM wave functions $\Phi_{k,L}$:

$$\Phi_{k,L} \equiv q_{kL} P_{00}^L \Phi^c(\mathbf{b}_k), \quad (\text{A18})$$

$$\tilde{\Phi}_{k,L} = \sum_{k'} A_{kk'}^{(L)} \Phi_{k',L}, \quad (\text{A19})$$

$$\langle \tilde{\Phi}_{k,L} | \tilde{\Phi}_{k',L} \rangle = \delta_{kk'}, \quad (\text{A20})$$

$$(\text{A21})$$

where q_{kL} are the normalization factors $q_{kL} \equiv 1/\langle P_{00}^L \Phi^c(\mathbf{b}_k) | P_{00}^L \Phi^c(\mathbf{b}_k) \rangle^{1/2}$. By using the partial wave expansion of the functions $\Gamma(\mathbf{r}, \mathbf{b}_k, \nu')$, the radial functions $\chi_L^{(k)}(r)$ in the k -th wave functions $\Phi_{k,L}$ can be expressed as follows:

$$\Phi_{k,L} = \frac{1}{\sqrt{(1+\delta_{C_1, C_2})} \begin{pmatrix} A \\ A_1 \end{pmatrix}} \mathcal{A} \{ \chi_L^{(k)}(r) Y_{L0}(\hat{r}) \phi_0(C_1) \phi_0(C_2) \}, \quad (\text{A22})$$

$$\chi_L^{(k)}(r) = n_0 q_{kL} \sqrt{\frac{2l+1}{4\pi}} \Gamma_L(r, b_k, \nu'), \quad (\text{A23})$$

$$\Gamma_L(r, b_k, \nu') = \left(\frac{2\nu'}{\pi}\right)^{3/4} 4\pi i_L(2\nu' r b_k) e^{-\nu'(r^2 + b_k^2)}, \quad (\text{A24})$$

where i_L is the modified spherical Bessel function. We assume that the projection operator P_L^c onto the cluster model space can be written by the orthonormal basis $\tilde{\Phi}_{k,L}$,

$$P_L^c = \sum_k |\tilde{\Phi}_{k,L}\rangle \langle \tilde{\Phi}_{k,L}| = \sum_{k,k',k''} |\Phi_{k',L}\rangle A_{kk'}^{(L)} A_{kk''}^{(L)*} \langle \Phi_{k'',L}|. \quad (\text{A25})$$

In this case, the radial function $\chi_L(r)$ in Eq.A7 for $\Phi_L(^{12}\text{Be})$ is written as

$$\chi_L(r) = \sum_k \chi_L^{(k)}(r) \left\{ \sum_{k,k''} A_{kk'}^{(L)} A_{kk''}^{(L)*} \langle \Phi_{k'',L} | \Phi_L(^{12}\text{Be}) \rangle \right\}. \quad (\text{A26})$$

2. Practical calculation of μ_{nL}

In the present calculations, we chose $b_k = 1, 2, \dots, 9$ fm for $L = 0, 2$ ($L = 0, 2, 4, 6$), $b_k = 2, 3, \dots, 9$ fm for $L = 4, 6$, and $b_k = 3, \dots, 9$ fm for $L = 8$ ($L = 8$) for the $^8\text{He} + ^4\text{He}$ ($^6\text{He} + ^6\text{He}$) channel.

In the practical calculations, the values μ_{nL} were obtained as follows. With the use of the expansion of $\chi_L^{(k)}(r)$ in the normalized cluster wave functions $\Phi_{k,L}$ by $R_{nL}(r, \nu')$

$$\chi_L^{(k)}(r) = \sum_n e_{nL}^{(k)} R_{nL}(r, \nu'), \quad (\text{A27})$$

μ_{nL} should be satisfy the following equations:

$$\sum_n e_{nL}^{(k)2} \mu_{nL} = 1 \quad . \quad (\text{A28})$$

The eigen values μ_{nL} equal to zero for the Pauli forbidden states with $N = 2n + L < N_{min}$ (N_{min} is the minimum allowed number) and $\mu_{nL} \sim 1$ with enough large numbers, $N = 2n + L$. In a practical calculation, we truncate the quanta n with a finite number $n = n_{min}, \dots, n_{max}$ ($N_{min} = 2n_{min} + L$, $N_{max} = 2n_{max} + L$) by assuming $\tilde{\mu}_{nL} = 1$ for $N = 2n + L > N_{max}$ to obtain approximated values $\tilde{\mu}_{nL}$ from Eq.A28. The approximated values $\tilde{\mu}_{nL}$ for simple systems, $\alpha + \alpha$ and $\alpha + ^{16}\text{O}$ are compared with the exact eigen values μ_{nL} in Table VIII.

In the present calculation of ^{12}Be , N_{max} was chosen to be 14. By using $\tilde{\mu}_{nL}$ determined by Eq.A28, we define the approximate R.W.A. $\tilde{y}_L(a)$ and the relative wave function $\tilde{u}_L(a)$ for $\Phi_L(^{12}\text{Be})$ by analogy with the relations in Eqs.A4 and A9:

TABLE VIII. The eigen values $\mu_{N=2n+L}$ and approximated values $\tilde{\mu}_{nL}(L=0)$ of the RGM norm kernel for $\alpha+\alpha$ and $\alpha+^{16}\text{O}$ systems. The values μ_N are taken from Ref. [29]. The width parameters for α and ^{16}O are assumed to be same.

N	$\alpha + \alpha$		N	$\alpha + ^{16}\text{O}$	
	μ_N	$\tilde{\mu}_{nL}$		μ_N	$\tilde{\mu}_{nL}$
0	0	0	0	0	0
2	0	0	2	0	0
4	0.7500	0.7500	4	0	0
6	0.9375	0.9375	6	0	0
8	0.9844	0.9844	8	0.2292	0.2292
10	0.9961	0.9962	10	0.5103	0.5063
12	0.9990	0.9987	12	0.7185	0.7538
			14	0.8459	0.7399
			16	0.9178	1
			18	0.9568	1
			20	0.9775	1
			22	0.9884	1
			24	0.9941	1
			26	0.9970	1

$$\tilde{y}_L(a) \equiv \sum_n e_{nL} \tilde{\mu}_{nL} R_{nL}(a, \nu'), \quad (\text{A29})$$

$$\tilde{u}_L(a) \equiv \sum_n e_{nL} \tilde{\mu}_{nL}^{1/2} R_{nL}(a, \nu'), \quad (\text{A30})$$

where the coefficients e_{nL} were calculated by $e_{nL} = \int r^2 \chi_L(r) R_{nL} dr$ from $\chi_L(r)$ given in Eq.A26. The cluster probability is estimated by

$$\tilde{S}_u \equiv \int r^2 \tilde{u}_L^2(r) dr = \sum_n e_{nL}^2 \tilde{\mu}_{nL}. \quad (\text{A31})$$